GEOPHYSICS, VOL. 56, NO. 4 (APRIL 1991); P. 496–518, 16 FIGS.

Analytic investigations of the effects of near-surface three-dimensional galvanic scatterers on MT tensor decompositions

R. W. Groom* and R. C. Bailey‡

ABSTRACT

An outcropping hemispherical inhomogeneity embedded in a two-dimensional (2-D) earth is used to model the effects of three-dimensional (3-D) near-surface electromagnetic (EM) "static" distortion. Analytical solutions are first derived for the galvanic electric and magnetic scattering operators of the heterogeneity. To represent the local distortion by 3-D structures of fields which were produced by a large-scale 2-D structure, these 3-D scattering operators are applied to 2-D electric and magnetic fields derived by numerical modeling to synthesize an MT data set. Synthetic noise is also included in the data.

These synthetic data are used to study the parameters recovered by several published methods for decomposing or parameterizing the measured MT impedance tensor. The stability of these parameters in the presence of noise is also examined. The parameterizations studied include the conventional 2-D parameterization (Swift, 1967), Eggers's (1982) and Spitz's (1985) eigenstate formulations, LaTorraca et al.'s (1986) SVD decomposition, and the Groom and Bailey (1989) method designed specifically for 3-D galvanic electric scattering. The relationships between the impedance or eigenvalue estimates of each method and the true regional impedances are examined, as are the azimuthal (e.g., regional 2-D strike, eigenvector orientation and local strike) and ellipticity parameters.

The 3-D structure causes the conventional 2-D estimates of impedances to be site-dependent mixtures of the regional impedance responses, with the strike estimate being strongly determined by the orientation of the local current. For strong 3-D electric scattering, the local current polarization azimuth is mainly determined by the local 3-D scattering rather than the regional currents. There are strong similarities among the 2-D rotation estimates of impedance and the eigenvalue estimates of impedance both by Eggers's and Spitz's first parameterization as well as the characteristic values of LaTorraca et al. There are striking similarities among the conventional estimate of strike, the orientations given by the Eggers's, Spitz's (Q), and LaTorraca et al.'s decompositions, as well as the estimate of local current polarization azimuth given by Groom and Bailey. It was found that one of the ellipticities of Eggers, LaTorraca et al., and Spitz is identically zero for all sites and all periods, indicating that one eigenvalue or characteristic value is linearly polarized. There is strong evidence that this eigenvalue is related to the local current. For these three methods, the other ellipticity differs from zero only when there are significant differences in the phases of the regional 2-D impedances (i.e., strong 2-D inductive effects), implying the second ellipticity indicates a multi-dimensional inductive response.

Spitz's second parameterization (U), and the Groom and Bailey decomposition, were able to recover information regarding the actual regional 2-D strike and the separate character of the 2-D regional impedances. Unconstrained, both methods can suffer from noise in their ability to resolve structural information especially when the current distortion causes the impedance tensor to be approximately singular. The method of Groom and Bailey, designed specifically for quantifying the fit of the measured tensors to the physics of the parameterization, constraining a model, and resolving parameters, can recover much of the information in the two regional impedances and some information about the local structure.

Manuscript received by the Editor November 20, 1989; revised manuscript received October 9, 1990.
*Formerly Department of Physics, University of Toronto; presently Geological Survey of Canada, 1 Observatory Crescent, Ottawa, Ont., Canada K1A 0Y3.
‡Geology and Physics Departments, University of Toronto, Toronto, Ont., Canada M5S 1A7.

INTRODUCTION

It is well known (Park, 1985; Jiracek, 1990) that small-scale, three-dimensional (3-D) surface inhomogeneities complicate the interpretation of magnetotelluric (MT) impedance data even when the regional structure is simple (either 1-D or 2-D). A number of decompositions of the impedance tensor have been developed to deal with such 3-D effects. General eight-parameter decompositions such as those developed by Eggers (1982), Spitz (1985), LaTorraca et al. (1986), and Yee and Paulson (1987) do not assume any particular structural geometry. Other methods such as those of Zhang et al. (1987), Bahr (1988), and Groom and Bailey (1989) assume a priori that the conductivity structure has a somewhat more limited geometry.

In this paper, a partially analytic solution is developed for the fields due to a particular class of 3-D conductivity structures. The conductivity model is that of a small hemisphere embedded in an otherwise 1-D or 2-D structure. For sufficiently low frequencies, the inductive response of the hemisphere can be ignored. Under this assumption, analytic solutions are developed for electric and magnetic galvanic scattering operators which mathematically describe the effects of the 3-D inhomogeneity. Using 1-D or 2-D numerical solutions and the analytic 3-D scattering operators, very accurate synthetic MT data at closely spaced sites can be derived with low computer requirements. Random numbers are added to simulate signal noise.

With the synthetic data, the effects of a class of small-scale, surficial, 3-D inhomogeneities on parameterizations of the impedance tensor can be investigated. The effect of signal noise on parameter determination can be studied as well. We first investigate the effects of such 3-D structures on the conventional 2-D parameterization (Swift, 1967) at two representative sites on the model surface. We then determine and compare the parameters obtained at one of these two sites by three decompositions, namely, those of Eggers (1982), Spitz (1985), and LaTorraca et al. (1986). We also investigated the usefulness of a method specifically designed to account for such structure, namely, the electric distortion parameterization method of Groom and Bailey (1989).

Other decompositions or methods are available, such as Zhang et al. (1987), Yee and Paulson (1987), and Bahr (1988). However, space limitations prevent a discussion of all methods studied, all the examined sites, and the natural extension of comparisons using actual field data.

GALVANIC SCATTERING DUE TO A CONDUCTING HEMISPHERE

A hemisphere (Figure 1) of uniform conductivity σ_2 embedded in a medium of conductivity σ_1 is the model of a small-scale surface inhomogeneity. The conducting media are enclosed above by an insulating half-space to represent the earth's atmosphere as (approximately) an insulator. The radius R of the hemisphere is much less than either the free-space EM wavelength or the skin depths at the frequencies considered. This restriction on the radius allows us to consider the inhomogeneity to be excited by a locally uniform horizontal electric field, whenever the body is sufficiently removed from any inhomogeneities in the host medium. (Here, "sufficient" depends upon the accuracy requirements.) In addition, the flux of the time-varying magnetic field through the hemisphere is considered to be sufficiently small to neglect any induced secondary electric fields (West and Edwards, 1985). The EM problem thus reduces to the problem of determining the electrostatic distortion by a hemisphere when excited by a uniform electric field and the anomalous magnetic field due to the resulting anomalous current distribution.

Electric field distortion due to a hemisphere

Consider the electrostatic effect of a conducting hemisphere in a uniformly conducting half-space (Figure 1) excited by a uniform static electric field $E_0\hat{x}$. The electric field is determined from a potential function f, such that

$$\mathbf{E} = -\nabla f. \tag{1}$$

The solution is extracted by symmetry from the similar electrostatic problem for a uniformly conducting sphere, in a homogeneous medium, excited by a constant static field (Ward, 1967). In a spherical coordinate system (r, θ, ϕ) with the origin at the center of the sphere, the potential is given by (Honkura, 1975)

$$f_i(r, \theta, \phi) = \left(-E_0 + \frac{Q}{R^3}\right) r \sin\theta \cos\phi, \quad r \le R \tag{2}$$

within the inhomogeneity and

$$f_e(r, \theta, \phi) = \left(-E_0 r + \frac{Q}{r^2}\right) \sin\theta \cos\phi, \quad r \ge R \tag{3}$$

outside the hemisphere but within the conducting half-space ($z \ge 0$).

$$Q = \frac{\sigma_2 - \sigma_1}{\sigma_2 + 2\sigma_1} E_0 R^3, \tag{4}$$

where $\varepsilon_0 Q$ is the induced electric dipole moment of the hemisphere.

The total electric fields within the hemisphere are given by the negative of the gradient of the potential (1, 2)

$$\mathbf{E}_i(x, y, z) = E_0\left(\frac{3\sigma_1}{\sigma_2 + 2\sigma_1}, 0, 0\right), \tag{5}$$

and outside the hemisphere but within the conducting medium ($z \ge 0$) (1, 3)

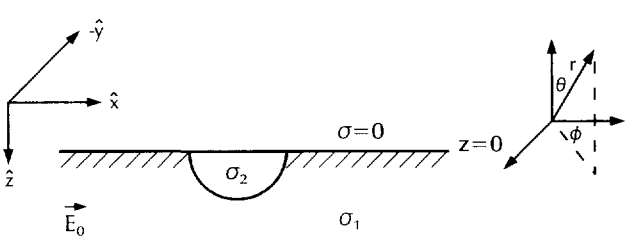

FIG. 1. Conducting hemisphere excited by a uniform electric field embedded in a homogeneous conducting half-space.

$$\mathbf{E}_e(x, y, z) = \left[E_0 + Q\frac{(2x^2 - y^2 - z^2)}{r^5}, \frac{3Qxy}{r^5}, \frac{3Qxz}{r^5}\right]. \quad (6)$$

Outside the hemisphere, the magnitude of the secondary electric field falls off as $(R/r)^3$. If the measurement site is $2R$ outside the hemisphere, the magnitude of the secondary electric field is approximately 4 percent of that of the primary electric field. Recalling that the radius of the hemisphere is very small compared to the EM skin depth, it is therefore clear that at low frequencies the geometric decay of the scattered electric fields is much more significant than phase rotation or amplitude loss due to diffusion in the host medium. The geometric falloff of the secondary electric field also dictates the distance that the lower dimensional boundaries must be from the hemisphere before the reflections of the scattered fields from these boundaries can be ignored for any particular accuracy requirement.

Magnetic field distortions due to a hemisphere

The previous solution for the distorted electric fields provides the means for determining the effects on the magnetic field from the anomalous current density $\mathbf{J}_a$ caused by the presence of the hemisphere.

Edwards et al. (1978) provided aspects of the solution for the electrostatic magnetic field due to an outcropping hemispherical depression from a grounded electrode source. We proceed by a quite different method to obtain the magnetic fields due to a uniform source field (details in the Appendix). The Appendix gives the solution as a sum of simple integrals. Although general analytic solutions for these integrals have not been found, the integrals are trivial to integrate numerically. The integral solutions are also used to indicate explicitly the symmetries in the fields (Appendix) which can reduce the numerical calculations.

Figure 2, which shows all components of the anomalous magnetic field for a primary electric field (E_0) in the x direction, illustrates the solution. In this example, the hemisphere has a radius of 100 m. For a given radius, the solution scales by a constant β which is dependent only upon the host, anomalous conductivity, and the primary electric field [i.e., $\beta = E_0\sigma_1(\sigma_2 - \sigma_1)/(\sigma_2 + 2\sigma_1)$].

In general, the anomalous horizontal magnetic field can be written as

$$\mathbf{H}_h^a = (\gamma\hat{\mathbf{x}} + \alpha\hat{\mathbf{y}})E_0. \quad (7)$$

We can determine analytically the anomalous magnetic field at the origin and thus determine the order of magnitude of the geometric factors γ and α. The solution for a primary field $E_0\hat{\mathbf{x}}$ is (Appendix):

$$\mathbf{H}_h^a(0, 0, 0) = -3\sigma_1\left(\frac{\sigma_2 - \sigma_1}{\sigma_2 + 2\sigma_1}E_0\right)\frac{R}{8}\mathbf{y}. \quad (8)$$

This is, in fact, the maximum magnitude of the surface horizontal anomalous magnetic field (Edwards et al., 1978). Therefore,

$$|\mathbf{H}_a(x_0, y_0, 0)| \le \frac{\sigma_1(\sigma_2 - \sigma_1)}{\sigma_2 + 2\sigma_1}\frac{E_0R}{2}\mathbf{y} \quad (9a)$$

$$= O(\sigma_1E_0R)\mathbf{y} \qquad [\sigma_1 \ne \sigma_2]. \quad (9b)$$

The proportionality constants (α, γ) are frequency independent geometric factors. Equations (9) imply that for a general 3-D scatterer these geometric factors are at most of order (σ_hL) where σ_h is the conductivity of the host and L is a characteristic scale length of the inhomogeneity. The electrostatic anomalous magnetic field also falls off sufficiently rapidly [equation (A-14)] due to geometric effects to neglect diffusion loss and phase rotation in the host medium.

The scattering tensors $\underline{C}$ and $\underline{D}$

The 3-D conducting hemisphere is now embedded in a larger structure. The *total* electric and magnetic fields at the surface of the conducting medium are now of interest as these comprise the magnetotelluric measurements. When the primary electric fields due to the large structure are approximately uniform over the hemisphere and the radius of the hemisphere is small compared to the relevant skin depths, the previous solutions give reasonable estimates of the effects of the hemisphere on the EM fields. The lateral and vertical boundaries of the large-scale structures must be sufficiently far from the hemisphere to ignore the backscattering of the secondary fields from the hemisphere. The assumption that no primary vertical electric field impinges on the hemisphere is reasonable since the normal electric field in the conducting medium must be zero at the interface with the insulator, and thus (except possibly near another inhomogeneity) the near-surface incident electric field (to a depth of one hemisphere radius) has a very small vertical component.

The primary electric field is defined here as the field that would exist if the hemisphere were not present. For an arbitrary but uniform and horizontal exciting field

$$\mathbf{E}_0 = (E_x^0, E_y^0),$$

the electric field (**E**) at the surface of the conducting medium is given by superposition and symmetry as

$$\mathbf{E}(x, y, 0) = \underline{C}\mathbf{E}_0. \quad (10)$$

The electric scattering tensor $\underline{C}$, termed the channeling tensor, is given by equation (5) as

$$\underline{C}_i(x, y, 0) = \begin{bmatrix} \dfrac{3\sigma_1}{\sigma_2 + 2\sigma_1} & 0 \\ 0 & \dfrac{3\sigma_1}{\sigma_2 + 2\sigma_1} \end{bmatrix} \quad (11)$$

inside the inhomogeneity and by equation (6)

$$\underline{C}_e(x, y, 0) = \begin{bmatrix} 1 + P\dfrac{(2x^2 - y^2)}{r^5} & \dfrac{P3xy}{r^5} \\ \dfrac{P3xy}{r^5} & 1 + P\dfrac{(2y^2 - x^2)}{r^5} \end{bmatrix} \quad (12)$$

outside the hemisphere where $P = R^3(\sigma_2 - \sigma_1)/(\sigma_2 + 2\sigma_1)$.

The rotational symmetry of the hemisphere about a vertical axis through its center is reflected by the fact that the distortion or scattering operator is symmetric (i.e., $C_{12} = C_{21}$) both inside and outside the hemisphere. $\underline{C}(x, y, 0)$ is therefore diagonalizable and has at most three independent

elements in the scattering matrix. This is a limitation of this model for such physical effects since the scattering operator can have as many as four independent elements.

When a symmetric 3-D scattering operator is combined with a 1-D regional structure, the impedance tensor has the form

$$\underline{Z} = \begin{bmatrix} C_{11} & C_{12} \\ C_{12} & C_{22} \end{bmatrix} \begin{bmatrix} 0 & Z_0 \\ -Z_0 & 0 \end{bmatrix} = Z_0 \begin{bmatrix} -C_{12} & C_{11} \\ -C_{22} & C_{12} \end{bmatrix}.$$

Thus the traditional skew ($Z_{11} + Z_{22}$) is zero and will be for all orientations of the measurement axes, which contradicts Yee and Paulson (1987). They asserted that when 3-D structures, having the symmetry of the hemisphere, are embedded in a horizontally layered earth, the impedance tensor is antisymmetric and the diagonal elements are equal.

Note some comparisons with the conclusions of Berdichevsky and Dmitriev (1976) who introduced a similar model. Inside the hemisphere, the channeling tensor has the form

$$\underline{C} = g \begin{bmatrix} 1 & 0 \\ 0 & 1 \end{bmatrix}, \tag{13}$$

and so the regional (1-D or 2-D) electric fields are scaled by a uniform factor g independent of frequency ("static shift"). Outside the hemisphere, along the principal axes of the 2-D structure (or the measurement axes if regional structure is 1-D), the channeling tensor has the form of an anisotropy operator as in the conclusions of Berdichevsky and Dmitriev (1976):

$$\underline{C} = \begin{bmatrix} 1 + s_1 & 0 \\ 0 & 1 + s_2 \end{bmatrix}. \tag{14}$$

Again the regional electric fields are scaled or shifted independent of frequency but by different factors. As the site

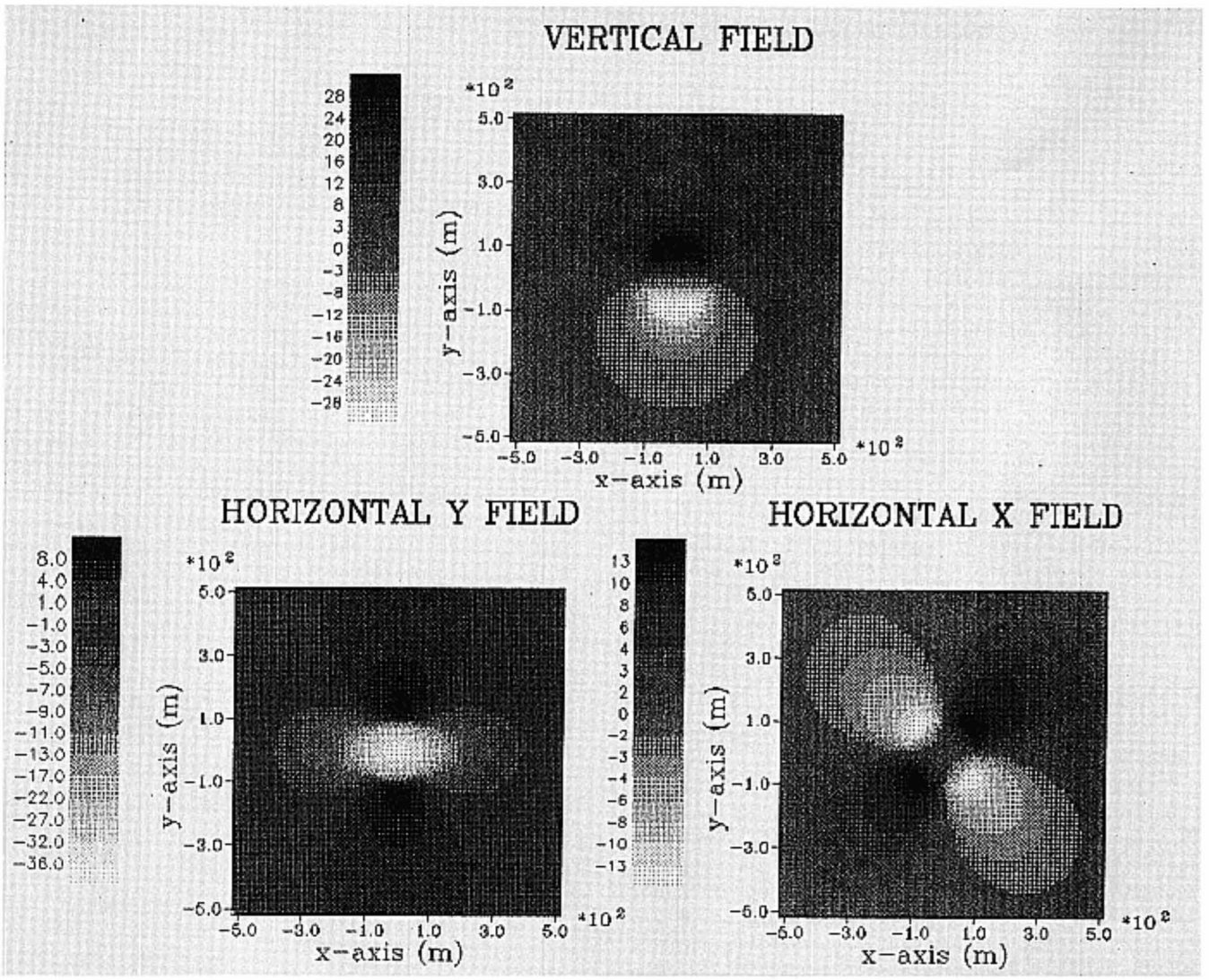

FIG. 2. Anomalous magnetic field: The x, y, and z components of an anomalous magnetic field due to electrostatic excitation of a hemisphere with a uniform electric field in the x direction (parallel to the horizontal axis). The amplitude is in meters. The solutions have been divided by the constant β, which has the units of current density (see text). The hemisphere is centered on (0, 0) and has a radius of 100 m.

changes azimuthally around the hemisphere, the distortion or scattering operator changes rapidly from this form of an anisotropy operator. A quite different form from equation (14) for $\underset{\sim}{C}$ is found along the lines $|x| = |y|$, outside the distorting body. Here

$$\underset{\sim}{C} = \begin{bmatrix} 1 + \dfrac{P}{2^{5/2}|x|^3} & \dfrac{3P}{2^{5/2}|x|^3} \\ \dfrac{3P}{2^{5/2}|x|^3} & \dfrac{P}{2^{5/2}|x|^3} \end{bmatrix}, \tag{15}$$

which can be written in the form

$$\underset{\sim}{C} = g\begin{bmatrix} 1 & e \\ e & 1 \end{bmatrix}. \tag{16}$$

The channeling tensor has the form of an elastic strain tensor where the shearing strains are equal and nonzero. This form of the channeling tensor will henceforth be called a "shear tensor." At sites exhibiting this type of distortion, the resulting components of the measured electric field are therefore linear combinations of the primary electric field components, i.e.,

$$E_x = g(E_x^0 + eE_y^0)$$

and

$$E_y = g(eE_x^0 + E_y^0).$$

In general, the 3-D electric scattering matrix causes the measured electric fields to be combinations of the regional electric fields. At sites on the principal axes [equation (14)], each component of the measured electric field is merely a multiple of that component of the regional field, which can be deceiving as being a possible class of effects. Just off the principal axes but near the edge of the hemisphere, the distortion operator has approximately the form

$$\underset{\sim}{C} = \begin{bmatrix} C_{11} & C_{12} \\ C_{12} & 0 \end{bmatrix}.$$

The y component of the measured field is a multiple of the regional x-component. An important case is when the local structure almost shorts the current flow in one direction, channeling that component of the regional current into the perpendicular direction. In this case,

$$\underset{\sim}{C} = \begin{bmatrix} C_{11} & C_{12} \\ 0 & 0 \end{bmatrix}.$$

If $|C_{11}| \gg |C_{12}|$, then information on the regional y component is virtually lost.

A magnetic channeling tensor $\underset{\sim}{D}$ for the distortion of the magnetic field can be defined in a manner similar to $\underset{\sim}{C}$. Equations (A-2), (A-8), and (A-9) give the anomalous horizontal magnetic field at an arbitrary field point, due to a uniform electric source field in the x direction. By similar calculations for a uniform source field in the y direction, it can be shown that the anomalous magnetic fields tangential to the surface $z_0 = 0$ and on that surface can be expressed as [equation (7)]

$$\mathbf{H}_h^a(x_0, y_0, 0) = \begin{pmatrix} \gamma & -\alpha \\ \beta & -\gamma \end{pmatrix}\mathbf{E}_0 = \underset{\sim}{D}\mathbf{E}_0. \tag{17}$$

The fact that there are only three independent elements in this channeling operator is a result of the symmetry of the scattering body. In general, four independent elements will be required to represent the magnetic scattering of an arbitrary 3-D inhomogeneity.

THE DISTORTED IMPEDANCE TENSOR

To extend this illustration to include the effects of small-scale inhomogeneities on MT interpretation and MT impedance tensor decomposition, consider a simple 2-D earth model such as the example in Figure 3. The 2-D structure together with the MT assumption of a plane-wave source field has two uncoupled modes of current flow. That is

$$\mathbf{E}_0 = \begin{pmatrix} 0 & Z_\perp \\ -Z_\parallel & 0 \end{pmatrix}\mathbf{H}_0 = \underset{\sim}{Z}_2\mathbf{H}_0 \tag{18}$$

when the measurement axes are parallel and perpendicular to the principal or strike axes of the 2-D structure. In the E polarization mode, the electric field is parallel to the vertical contact and this results in an impedance $Z_\parallel$. While in the H polarization mode, the horizontal electric field is perpendicular to the contact and thus the impedance is termed $Z_\perp$.

In this simple 2-D earth model, a conducting hemisphere (R = 100 m) is embedded 6 km to the left of the vertical contact (Figure 4). For the frequencies used, the hemisphere is sufficiently removed from the faults to ensure that the primary electric fields (due to the 2-D structure) are uniform over the extent of the hemisphere. Due to the small size of the hemisphere, one can neglect, except as a minor effect, any induced secondary fields produced by the small inhomogeneity. At the frequencies utilized in this example (≤3000 Hz), the galvanic response of the hemisphere dominates the inductive response. (The channeling number σ_2/σ_1 is 30, while at 1000 Hz, the induction number $\sigma_2\mu_0\omega R^2$ is only 8.) Even at the highest frequency (3000 Hz), where the 3-D inductive response has some significance and the solution given here is only a partial solution, our solution is sufficient for illustrating some important points. In addition, it can be verified that the hemisphere is sufficiently removed from any of the 2-D model boundaries to neglect backscattering.

The total fields can be expressed as [Equations (10), (17), (18)]

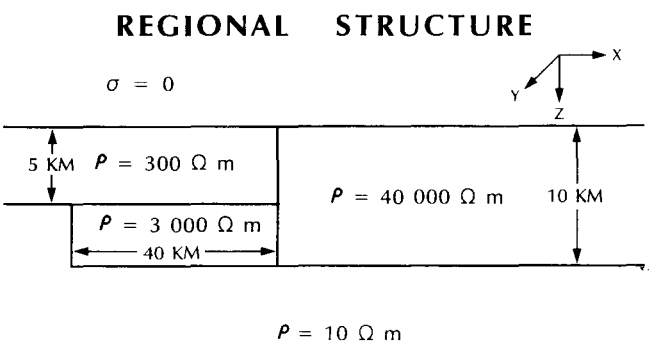

FIG. 3. Regional conductivity structure: The regional 2-D structure.

$$\mathbf{E} = \underline{C}\mathbf{E}_0$$

$$\mathbf{H} = \mathbf{H}_0 + \underline{D}\mathbf{E}_0$$

$$= (\underline{I} + \underline{D}\underline{Z}_2)\mathbf{H}_0 \tag{19}$$

and thus

$$\mathbf{E} = \underline{C}\underline{Z}_2\mathbf{H}_0 \tag{20a}$$

$$= \underline{C}\underline{Z}_2(\underline{I} + \underline{D}\underline{Z}_2)^{-1}\mathbf{H}. \tag{20b}$$

The observed impedance tensor is therefore given by

$$\underline{Z} = \underline{C}\underline{Z}_2(\underline{I} + \underline{D}\underline{Z}_2)^{-1} \tag{21a}$$

$$= \underline{C}\underline{Z}_2\left[\underline{I} + \begin{pmatrix} \gamma & -\alpha \\ \beta & -\gamma \end{pmatrix}\underline{Z}_2\right]^{-1}. \tag{21b}$$

The elements of $\underline{D}$, α, γ/β [equation (17)] are given by the integral equations (A-2), (A-8), and (A-9).

Equation (21) indicates that while the electric effects of the inhomogeneity are frequency independent, the magnetic effects are not. The elements of $\underline{D}\underline{Z}_2$ have magnitude [equation (9)]

$$\sigma_h R\sqrt{\mu_0\omega\rho_a} \to 0 \qquad \text{as } \sqrt{\omega} \to 0, \tag{22}$$

where σ_h is the host conductivity and ρ_a is the apparent resistivity of the 2-D structure at the considered frequency. The limit assumes, as is reasonable, that the apparent resistivity (ρ_a) remains bounded as the frequency decreases. In general the elements of $\underline{D}\underline{Z}_2$ have magnitude less than one and thus

$$\underline{Z} \approx \underline{C}\underline{Z}_2[\underline{I} - \underline{D}\underline{Z}_2] \tag{23a}$$

$$= \underline{C}[\underline{I} - \underline{Z}_2\underline{D}]\underline{Z}_2. \tag{23b}$$

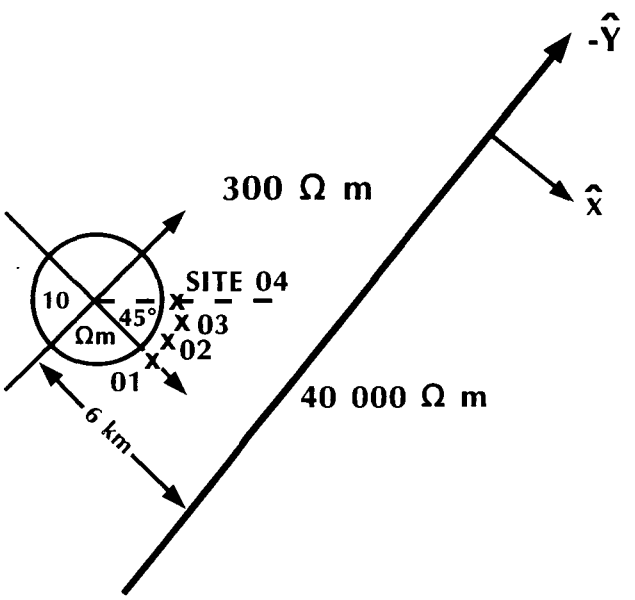

FIG. 4. Plan view of conductivity geometry: A plan view of the hemisphere embedded in the 2-D regional structure. The test sites are indicated.

Once the magnetic effects are included, the full galvanic distortion or scattering operator ($\underline{C}[\underline{I} - \underline{Z}_2\underline{D}]$) is complex and frequency dependent. If one includes 3-D inductive effects, the resulting scattering operator is more complicated (Groom, 1988), still consisting of a static real component but with multiple complex components all of which decay with decreasing frequency.

The scattering operators $\underline{C}$ and $\underline{D}$ are coordinate dependent (i.e., linear transformations) as is the regional impedance tensor $\underline{Z}_2$. Therefore, as a frame of reference, we choose to express these tensors in the regional or principal coordinate frame; the impedance tensor is therefore given by the relation

$$\mathbf{E} = \underline{R}(\theta)\underline{C}\,[\underline{I} - \underline{Z}_2\underline{D}]\,\underline{Z}_2\underline{R}^t(\theta)\mathbf{H}, \tag{24a}$$

where $\underline{R}(\theta)$ is a rotation from the principal axes to the measurement axes and $\underline{R}^t$ is the transpose (and inverse) of the rotation tensor.

No matter what decomposition is used, extraction of parameters amounts to inverting the data ($\underline{Z}$) for a set of parameters which are governed by a system which in general is nonlinear. How close the determinant of the transformation is to zero usually determines what information can be extracted and how stable are the resulting parameters in the presence of noise. Here,

$$\det \underline{Z} \approx \det(\underline{C}) \det(\underline{Z}_2). \tag{24b}$$

Only in very special cases will the determinant of $\underline{Z}_2$ be zero. However, for strong galvanic scattering, the determinant of $\underline{C}$ is often near zero. For example, when the hemisphere is much more conducting than the host and near the outside edge of the hemisphere, det $\underline{C} \approx 0$. As equation (24) shows, the singularity of the transfer function is not modified by the choice of measurement system. The presence of noise is therefore a factor in parameter determination, especially when the impedance tensor is nearly singular.

The synthetic test data

Synthetic impedance tensor data can be generated quite simply and accurately given the above solutions and derived relations. The 2-D impedance tensors (e.g., Figure 5) of the chosen regional structure were determined by a numerical modeling program (Madden and Thompson, 1965). In the 3-D examples discussed here, it was assumed for simplicity that the measurement axes were parallel and perpendicular to the strike of the regional 2-D structure [$\theta = 0$ in equation (24)]. Noise was thus systematically added to the synthetic tensor data to study its effects on the estimation of parameters in a tensor decomposition. Simplistically, normal random noise was added with a standard deviation of 2 percent of the largest element in the impedance matrix. The *measurement* sites used here are all 1 m outside the hemisphere, producing strong effects to illustrate clearly the 2-D regional responses (Figure 5) are essentially identical at all sites.

Not only the usefulness but also the limitations of this set of synthetic data are important. As mentioned, the symmetry of the hemisphere produces scattering operators $\underline{C}$ and $\underline{D}$, which have particular symmetries (equations (11), (12), (17)]. In addition, the 3-D models are limited in having no 3-D inductive response. From our experience with field data,

probably the most important limitation is that the 3-D effects are present throughout the frequency band with only the 2-D effects changing with increasing period. Realistically, as the period increases, the 2-D structure becomes increasingly more 3-D and the nature of the 3-D effects changes during this transition. The second most important limitation, in comparison to field data, is that the noise has similar attributes throughout the entire frequency range.

INVESTIGATION OF DECOMPOSITION METHODS

Conventional 2-D parameterization

The most common method for interpreting the measured impedance tensor is to assume that it has the form

$$\underline{Z}_m = \underline{R}\begin{bmatrix} s_1 & 0 \\ 0 & s_2 \end{bmatrix}\underline{Z}_2\underline{R}^t. \tag{25}$$

In other words, it is assumed that the principal impedances $(Z_\parallel, Z_\perp)$ can be obtained by rotating the impedance tensor to an off-diagonal form (diagonal elements zero) and extracting the principal impedances albeit scaled by real factors (s_1, s_2) or "static shifts" as they are sometimes called.

Since the data include noise, stable implementation of this method requires some manipulation of the data such as rotating the measured impedance tensor $(\underline{Z}_m)$, $\underline{Z}' = \underline{R}\underline{Z}_m\underline{R}^t$, so that the sum of the square of magnitudes of the diagonal elements is minimized (Swift, 1967). The off-diagonal elements of $\underline{Z}'$ are extracted as estimates of $Z_\parallel$ and $Z_\perp$. Thus $\underline{Z}_m$ is estimated to be given by five real parameters through a nonlinear relation, i.e.,

$$\hat{\underline{Z}} = \underline{R}\begin{bmatrix} 0 & \hat{Z}_\parallel \\ -\hat{Z}_\parallel & 0 \end{bmatrix}\underline{R}^t. \tag{26}$$

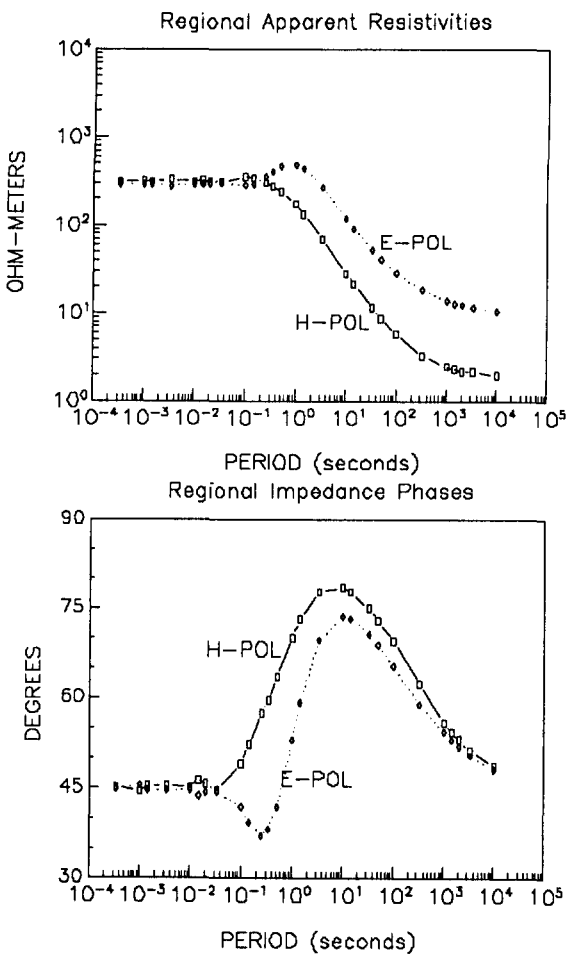

FIG. 5. Regional impedances: The complex E and H polarization impedances due to the underlying 2-D conductivity structure are displayed as apparent resistivities and phases of the impedances.

Compare the 2-D regional impedances plotted as apparent resistivity and phase in Figure 5 with Figure 6 which presents the 2-D parameterization of the synthetic data at site 01 (Figure 4). Site 01 is on a symmetry axis of the regional structure. As a result of this and the symmetry of the hemisphere, the distortion effects are of a special nature. The electric channeling tensor at site 01 is a diagonal operator [equation (14)] as is the magnetic distortion tensor. The resulting impedance tensor therefore has the form of equation (25) and cannot be distinguished from an impedance tensor due only to a 2-D structure. Under the conventional 2-D parameterization (Figure 6), the regional strike direction has been determined correctly; the skew is zero; the impedance magnitudes have the shape of the regional apparent resistivities; and the impedance phases are regional phases except at the higher frequencies where magnetic effects cause distortions of almost 15 degrees. (The traditional skew is plotted here as an angle which is simply the arctangent of the skew.)

Note from Figure 6 that, as in later figures, the parameter error bars are not always centered on the symbol. In all the figures, a symbol represents the value of the parameter determined from the mean impedance tensor which for this paper is the synthetic data with only computer roundoff errors. The error bars represent the spread of the parameter value once the synthetic noise has been added. In general, the parameters are nonlinear functions of the data, and thus noise can bias a parameter estimate and as such the error bars will not generally be symmetric about the estimate from the mean data. When the noise bias is sufficiently strong, the error bars will not include the estimate from the mean. For this data set, det $\underline{C} \approx 1/3$, and therefore the magnitude of the determinant of the impedance tensor is reduced by this factor from that of the regional impedance tensor. As a result, the minor impedance parameter is quite erratic when noise is added.

To quantify the parameter representation of a measured tensor, the normalized least-squares fit of the estimated impedance to the synthetic impedance is also given in Figure 6. The root-mean-square (rms) relative error of fit ε is given by

$$\varepsilon^2 = \frac{\sum_{i=1}^{2}\sum_{j=1}^{2}|\hat{Z}_{ij} - Z_{ij}|^2}{\sum_{i=1}^{2}\sum_{j=1}^{2}|Z_{ij}|^2}, \tag{27}$$

where Z_{ij} and $\hat{Z}_{ij}$ are, respectively, the measured and modeled [e.g., equation (26)] impedance tensor elements. The rms error parameter ε should be small compared with unity if the model of the impedance tensor is adequate. The value of ε in the synthetic data without any noise present (squares in Figure 6) indicates the accuracy of the calculations if the model is correct. In this figure, at the long periods where there are almost no significant magnetic effects, ε is at the numerical precision level of the computer. While at high frequencies, ε indicates the accuracy of the numerical integration for the magnetic effects. With sufficient noise in the data, ε is the relative noise level. In this case, the relative noise level is 2 percent as indicated by the error bars in the small rms figure (Figure 6).

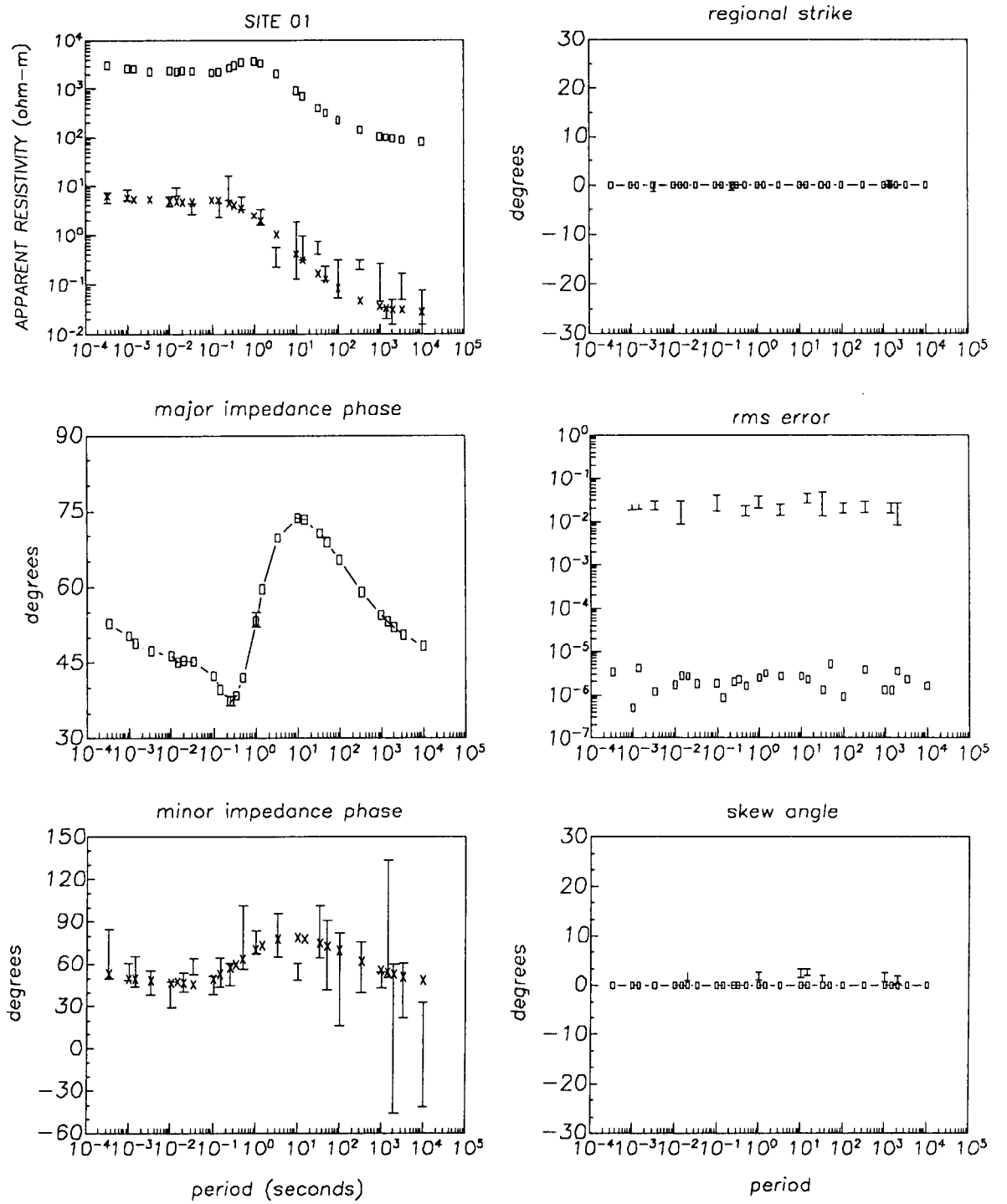

FIG. 6. 2-D parameterization at site 01: The principal 2-D apparent resistivities, impedance phases, strike angle, skew angle, and normalized least-squares error of fit [equation (27)].

Another interesting site and the one used throughout the remainder of this paper is site 04 at 45 degrees to the coordinate axes. The diagonal elements of the channeling matrix are equal here [$e \approx 1$, equation (16)] and the off-diagonal terms are nonzero. This can be seen graphically in Figure 7 where the synthetic data are presented for this site. Note that the *measured* impedance tensor in the presence of the inhomogeneity no longer has only off-diagonal elements, even when the measuring axes correspond to the 2-D structure. At longer periods, the components Z_{xy} and Z_{yy} of $\underline{\mathbf{Z}}_m$ have the form of $Z_{\parallel}$ although scaled by slightly different real coefficients. Similarly, Z_{xx} and Z_{yx} have the form of $Z_{\perp}$. At short periods, the 3-D magnetic effects cause the phases of the impedance elements to vary considerably from the regional phases.

Due to our procedure for adding the noise, the elements of the first column of the data (Z_{xx}, Z_{yx}) have proportionally more noise added than the larger elements in the second column.

Figure 8 contains the 2-D parameterization of the measured data obtained by the conventional means of rotating to the supposed strike direction. There are a number of interesting results evident from Figure 8. Note how unstable the estimate of the minor impedance is when determined by rotation to strike. Notice also that the conventional method produces an erroneous estimate of the regional strike (0 degrees). The Swift method produces an azimuth of about 35 degrees at long periods, increasing to 45 degrees at short periods. Note how the minor impedance phase results in Figure 8 move smoothly and rapidly out of the first quadrant as the period increases. (This phenomenon of phases occurring out of their expected quadrant also occurred for synthetic 1-D regional data when the 3-D distortion was sufficiently strong.)

To illustrate that the conventional estimate of regional strike azimuth is determined by local scattering, Figure 9 indicates the nature of the variation in the regional azimuth by the conventional method at three different sites. At high frequencies, the regional response is essentially one-dimensional. At such frequencies, some simple calculations [equation (12)] show that, at any site just outside the hemisphere and at an angle θ to the coordinate system, the direction of the local electric field and thus the local current is approximately θ. At long periods the local strike (local electric field polarization azimuth) should vary only slightly from this angle. It appears (Figure 9) that the conventional method tends to pick out the direction of the local current polarization azimuth (the orientation of the major axis of the local current ellipse).

Figure 8 also permits comparisons of the apparent resistivities and impedance phases with the 2-D undistorted principal impedances (Figure 5). The principal impedances of $\underline{\mathbf{Z}}_m$ have the form of neither $Z_{\parallel}$ nor $Z_{\perp}$ but rather are mixtures of them. To discuss this mixing, it is convenient to introduce a modified form of a set of basis matrices termed the Pauli spin matrices:

$$\underline{\mathbf{I}} = \begin{bmatrix} 1 & 0 \\ 0 & 1 \end{bmatrix} \qquad \underline{\boldsymbol{\Sigma}}_1 = \begin{bmatrix} 0 & 1 \\ 1 & 0 \end{bmatrix} \tag{28a}$$

$$\underline{\boldsymbol{\Sigma}}_2 = \begin{bmatrix} 0 & -1 \\ 1 & 0 \end{bmatrix} \qquad \underline{\boldsymbol{\Sigma}}_3 = \begin{bmatrix} 1 & 0 \\ 0 & -1 \end{bmatrix}. \tag{28b}$$

The data $\underline{\mathbf{Z}}_m$ can be represented (Spitz, 1985) as

$$\underline{\mathbf{Z}}_m = \frac{1}{2}(\alpha_0 \underline{\mathbf{I}} + \alpha_1 \underline{\boldsymbol{\Sigma}}_1 + \alpha_2 \underline{\boldsymbol{\Sigma}}_2 + \alpha_3 \underline{\boldsymbol{\Sigma}}_3), \tag{29}$$

where the α_i coefficients are determined from the elements Z_{ij} of $\underline{\mathbf{Z}}_m$ by

$$\alpha_0 = Z_{11} + Z_{22}, \tag{30a}$$

$$\alpha_1 = Z_{12} + Z_{21}, \tag{30b}$$

$$\alpha_2 = Z_{21} - Z_{12}, \tag{30c}$$

and

$$\alpha_3 = Z_{11} - Z_{22}. \tag{30d}$$

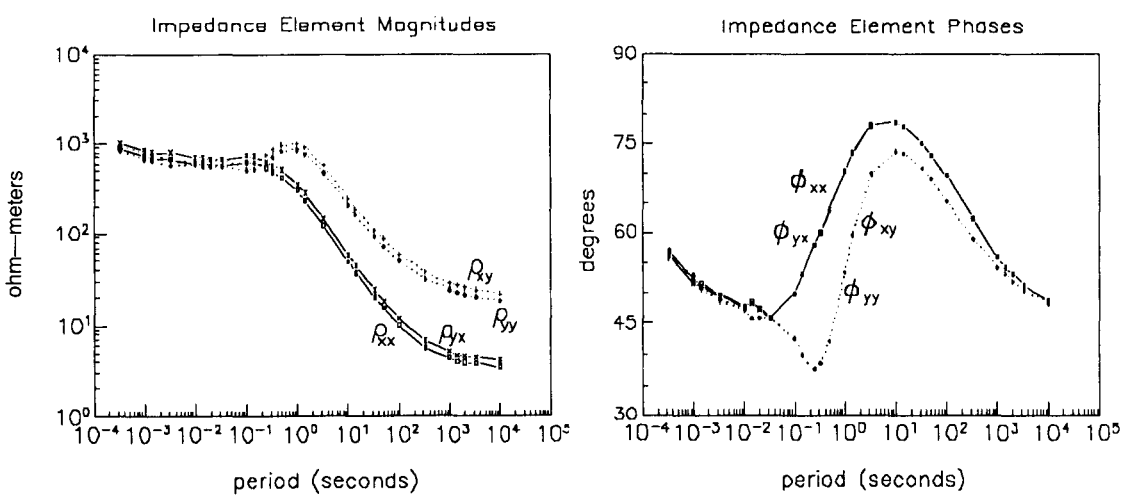

FIG. 7. Impedance data at site 04: The four complex elements of the impedance data at site 04 are plotted in the form of apparent resistivities and phases. In either column, the phases of the two elements are almost identical until the higher frequencies.

If one assumes the conductivity structure is 2-D, then the impedance tensor is merely a rotation by an angle θ of a tensor with zero diagonal elements [equation (18)]. In this case, the Pauli spin coefficients [equations (30)] would be given by a set of algebraic equations

$$\alpha_0 = 0, \tag{31a}$$

$$\alpha_1 = \delta \cos 2\theta, \tag{31b}$$

$$\alpha_2 = -\sigma, \tag{31c}$$

$$\alpha_3 = -\delta \sin 2\theta, \tag{31d}$$

where

$$\sigma = Z_{\parallel} + Z_{\perp} \quad \text{and} \quad \delta = Z_{\parallel} - Z_{\perp} \tag{32}$$

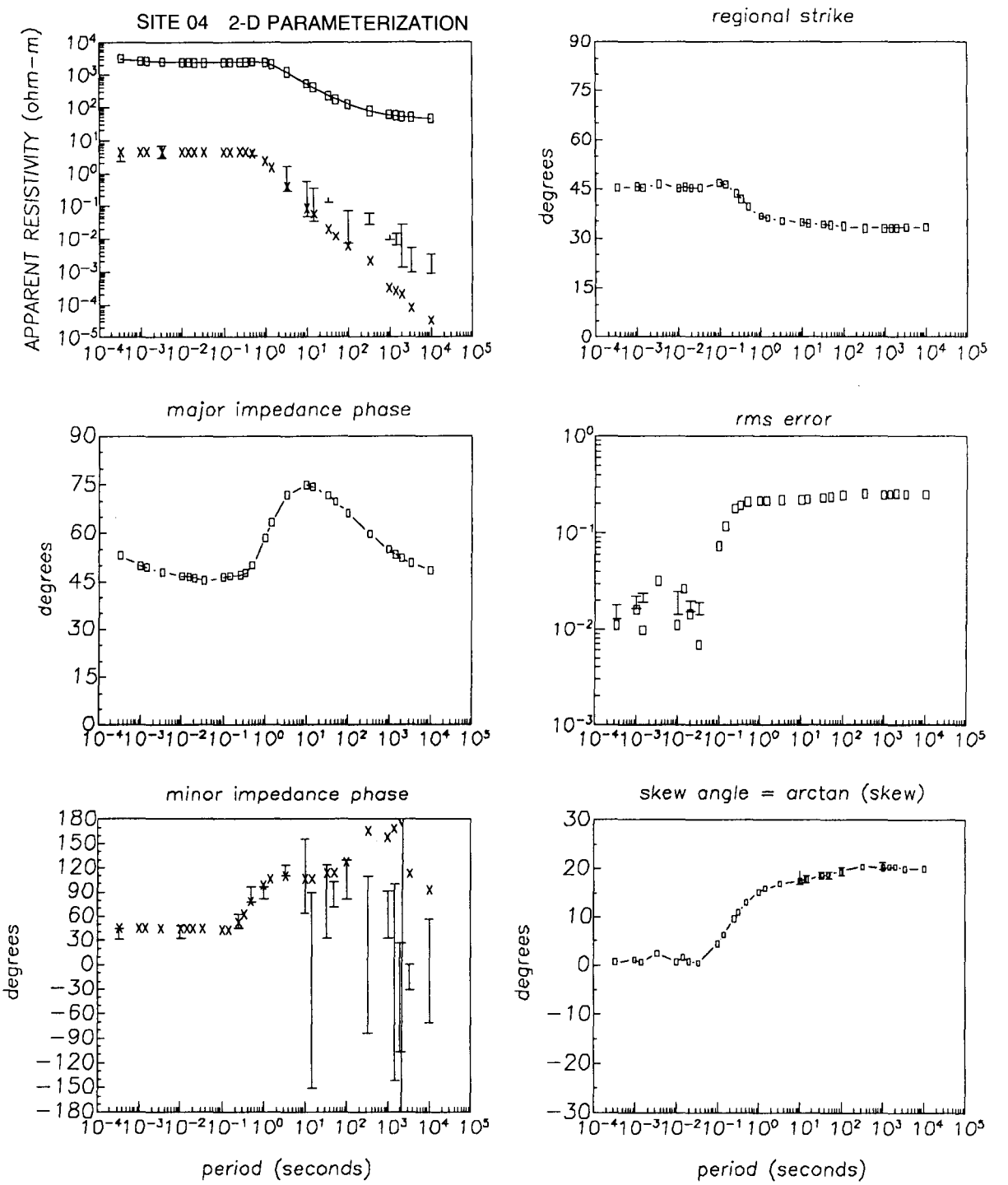

FIG. 8. 2-D estimates of impedance for site 04: Conventional 2-D strike, resulting off-diagonal impedances after rotation to strike, the conventional skew angle, and the least-squares norm of the data to the 2-D model (i.e., rms error).

are used for the sum of the principal impedances and their difference.

From equations (31) and (32), simple algebra indicates how to recover 2-D impedance estimates, i.e.,

$$\hat{Z}_{\parallel}, \hat{Z}_{\perp} = -\frac{\alpha_2}{2} \pm \frac{1}{2}\sqrt{\alpha_2^2 - 4 \det |\underline{\mathbf{Z}}_m|}. \qquad (33)$$

These are rotationally invariant estimates of the 2-D impedances since α_2 and the determinant are both rotationally invariant. These impedances are in fact Eggers's (1982) eigenvalues as reviewed below. Since both α_2 and the determinant in a 3-D geometry are functions of the elements of the scattering operators [equations (23) and (30)], these impedance elements are local site-dependent combinations of the regional impedances.

The algebraic estimates and those obtained by determining strike and then rotating to strike coordinates are equivalent in a perfectly 2-D situation. With the addition of noise, the two different estimates are virtually equivalent except the algebraic estimates are generally more stable. For a general 3-D structure, the similarity between the rotation estimates and the algebraic depends upon the particular structure and the signal noise. However, rotating to minimize the sum of the magnitudes of the diagonal elements is equivalent to minimizing α_3. Thus, it is easy to show that the algebraic and rotation estimates will differ significantly only when this minimization is relatively unsuccessful and the skew is large. However, the algebraic estimates are rotationally invariant and thus are not dependent upon a possibly incorrectly determined strike angle. Finally, and most important for the discussion here, equation (33) indicates algebraically how the 2-D principal regional impedances are mixed when there are 3-D static effects.

Figure 10 gives the algebraic 2-D impedance estimates at site 04. First note, by comparing Figures 8 and 10, that the stable major apparent resistivity and impedance phase estimates determined either by rotation or algebraically are virtually identical. At short periods, the minor impedance estimates are also equivalent. At longer periods, when the minor impedance estimate becomes very small and very unstable by the rotation method, the algebraic estimate remains relatively stable. The instability of the minor impedance, as estimated by rotation, is due to the H polarization impedance magnitude being significantly smaller than the E polarization impedance. Combined with the small determinant of $\underline{\mathbf{C}}$, this results in the determinant of $\underline{\mathbf{Z}}$ being significantly smaller, relative to the noise, than at shorter periods.

Figure 10 clearly shows how the regional impedances have been so severely mixed as not to show the separate character of the two regional impedances. The algebraic apparent resistivities (without noise) have almost identical shapes and the impedance phases (without noise) are almost identical except in the very shortest periods where there are galvanic magnetic effects. Conventional wisdom might suggest these results arise from a 1-D environment contaminated by "static shift."

Thus, the mixing of the regional 2-D impedances by a small inhomogeneity could result in wrong structural inter-

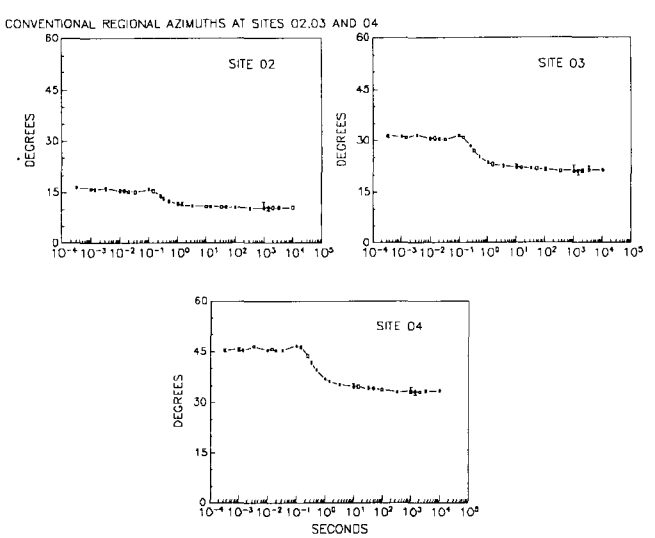

FIG. 9. Conventional azimuths: The conventionally calculated azimuths at sites 02, 03, and 04 (Figure 4).

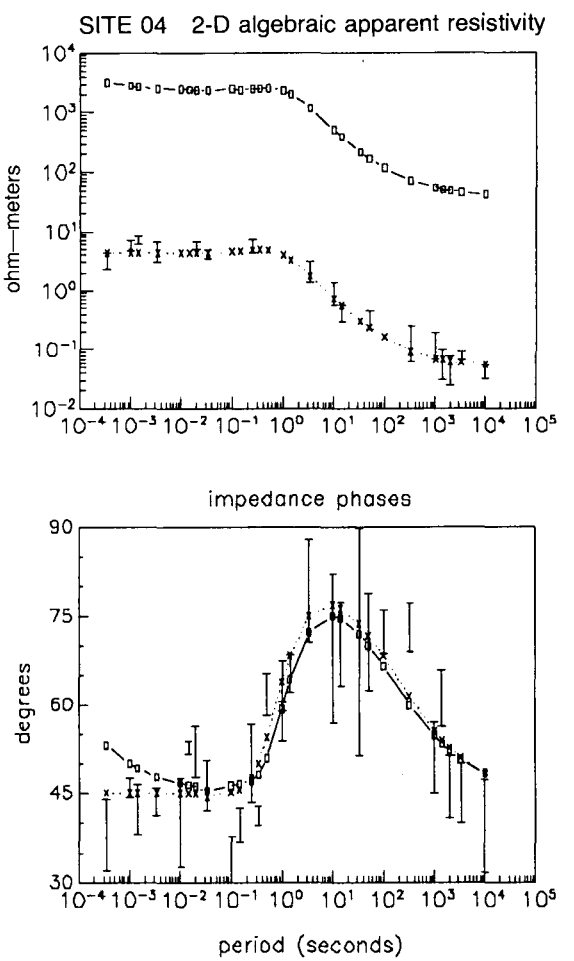

FIG. 10. Algebraic 2-D estimates: The algebraic estimates of principal 2-D impedances. Error bars shown in the phase are associated with the minor or minimum apparent resistivity. The errors in the phase of the major impedance are so small as to be indistinguishable from the associated symbols.

pretations. These structural interpretations are dependent upon the position of the measuring site with respect to the hemisphere (Figures 6 and 10). For this set of data, site 04 is at nearly the worst angle for this mixing; here the electric channeling tensor has the form of equation (16) rather than the diagonal form it has on the principal axes (i.e., site 01). The mixing may cause the interpreter to miss the 2-D induction in the data. Due to the mixing and the magnetic effects in the high frequencies, 1-D inversion of either of the resulting impedances can lead to difficulties even when shifting the resulting impedance magnitudes to fit known or hypothesized upper or lower conductivities. (These aspects will be discussed in a later paper.)

Eight parameter decompositions

The conventional analysis as previously discussed uses only five real parameters to describe the possible eight independent data at each period. We move now to some new methods for describing the data which extract eight parameters from the complex 2 × 2 impedance tensor.

Although our studies examined four of these new decompositions and sites at 15-degree increments around the hemisphere and at various radial distances from its center, space limitations allow us to examine briefly three of the eight parameter decompositions and only one site. Site 04 was chosen because it distinctly illustrates most of the important results.

Eggers's eigenstate formulation

Eggers (1985) defined impedance tensor eigenstates by

$$\mathbf{E}^{\pm} = \underline{\Lambda}^{\pm}\mathbf{H}^{\pm} \tag{34}$$

where

$$\underline{\Lambda}^{\pm} = \begin{bmatrix} 0 & \lambda^{\pm} \\ -\lambda^{\pm} & 0 \end{bmatrix}. \tag{35}$$

The scaler product between each electric eigenstate and its associated magnetic eigenstate vanishes and the eigenstates are related to the measured impedance data by

$$\mathbf{E}^{\pm} = \underline{\mathbf{Z}}_m\mathbf{H}^{\pm}. \tag{36}$$

The two complex eigenvalues are four of Eggers's eight real parameters. These eigenvalues are given by

$$\lambda^{\pm} = -\frac{\alpha_2}{2} \pm \frac{1}{2}\sqrt{\alpha_2^2 - 4 \det |\underline{\mathbf{Z}}_m|} \tag{37}$$

which, of course, is the algebraic equation for determining the 2-D estimates of impedance [equation (33)].

Figure 11 plots both the magnitudes of the eigenvalues as apparent resistivities and the complex phases as a function of period with errors. The orientations of the major axes for the polarization ellipses of the two electric eigenvectors ($\mathbf{E}^{\pm}$) are plotted along with their ellipticities. These constitute the four remaining parameters.

LaTorraca et al.'s SVD formulation

LaTorraca et al. (1986) expand the measured data as a product of three complex matrices

$$Z_m = \underline{\mathbf{U}}_E\{\mathbf{e}_1, \mathbf{e}_2\}\underline{\mathbf{M}}\underline{\mathbf{U}}_M^{\dagger}\{\mathbf{h}_1, \mathbf{h}_2\}, \tag{38}$$

where

$$\underline{\mathbf{M}} = \begin{bmatrix} \mu_1 & 0 \\ 0 & \mu_2 \end{bmatrix} \tag{39}$$

is a diagonal matrix of "characteristic" values and $\mathbf{e}_i$, $\mathbf{h}_i$, the "characteristic" vectors, are column vectors such that

$$\mathbf{h}_1 = \mathbf{v}(\beta_H, \gamma_H), \qquad \mathbf{h}_2 = \mathbf{v}\left(-\beta_H, \gamma_H \pm \frac{\pi}{2}\right) \tag{40a}$$

and

$$\mathbf{e}_1 = \mathbf{v}(\beta_E, \gamma_E), \qquad \mathbf{e}_2 = \mathbf{v}\left(-\beta_E, \gamma_E \pm \frac{\pi}{2}\right). \tag{40b}$$

Here a complex vector is given by

$$\mathbf{v}(\beta, \gamma) = (\cos\gamma\hat{\mathbf{x}} + \sin\gamma\hat{\mathbf{y}})\cos\beta + i(-\sin\gamma\hat{\mathbf{x}} + \cos\gamma\hat{\mathbf{y}})\sin\beta, \tag{41}$$

where γ is the orientation of the major axis of the ellipse of the time-domain vector [i.e., Re $(\mathbf{v}e^{-iwt})$] and β is the ellipticity of the time-domain ellipse.

Figure 12 is a plot of the characteristic values as a function of period for site 04. The orientations (γ) of the major axis for the ellipse of one of the electric vectors $\mathbf{e}_i$ and one of the magnetic vectors $\mathbf{h}_i$ are also plotted along with the tangent of the associated ellipticity β. LaTorraca et al. also define a "skew angle" (Figure 12) by

$$S = \frac{\pi}{2} - \gamma_H + \gamma_E. \tag{42}$$

Spitz's (1985) intrinsic coordinate system formulation

This method is based on Cayley factorization of the measured impedance tensor. The data factor as

$$\underline{\mathbf{Z}}_m = \underline{\mathbf{Q}}\underline{\mathbf{U}}, \tag{43}$$

where $\mathbf{Q}$ is positive definite and $\underline{\mathbf{U}}$ is unitary.

Two intrinsic coordinate systems are defined, the first (θ_1) by $\mathbf{Q}$ and the second (θ_2) by $\underline{\mathbf{U}}$. The data are rotated to each of these frames and expanded thus:

$$\hat{\underline{\mathbf{Z}}}_m(\theta_i) = \begin{bmatrix} \alpha_0 & 0 \\ 0 & \alpha_0 \end{bmatrix} + \begin{bmatrix} 0 & \lambda_1 \\ -\lambda_2 & 0 \end{bmatrix} + \begin{bmatrix} \alpha_3(\theta_i) & 0 \\ 0 & -\alpha_3(\theta_i) \end{bmatrix}. \tag{44}$$

This defines two impedances or eigenvalues for each intrinsic coordinate system, $\lambda_1 = \alpha_1(\theta_i) - \alpha_2$, $\lambda_2 = -\alpha_1(\theta_i) - \alpha_2$. [We have used our notation for the Pauli spin coefficients, equation (30), rather than that of Spitz.]

The two eigenvalues for site 04 are plotted in Figure 13 as functions of period for the intrinsic coordinate system due to $\mathbf{Q}$ and in Figure 14 for the coordinate system due to $\underline{\mathbf{U}}$. Each figure contains a plot of the rotation angle (θ_i) defining the system. Spitz also defines indicators of dimensionality by the ellipticities

$$\varepsilon_i = \frac{|\hat{Z}_{11}(\theta_i) - \hat{Z}_{22}(\theta_i)|}{|\hat{Z}_{12}(\theta_i) + \hat{Z}_{21}(\theta_i)|}, \tag{45}$$

which are also plotted in Figures 13 and 14. Spitz also suggests that $\alpha_0(Z_0)$ and

$$\mathrm{Im}\,[\alpha_1^*, \alpha_3]$$

are indicators of three-dimensionality. These indicators are also plotted in Figure 13. Our studies with 3-D synthetic data have not confirmed Spitz's (1985) assumptions concerning these dimensionality indicators. Since the 3-D magnetic effects have all but vanished below 10 Hz, the data at site 04 at long periods have at most six degrees of freedom [equation (23)] not including the noise (i.e., $C_{11} = C_{22}$, $C_{12} = C_{21}$ and the two complex regional impedances). At the longest periods there are only five degrees of freedom since the regional impedances have essentially the same phase. However, as seen in the lower section of Figure 13, neither 3-D indicator vanishes below 10 Hz as Spitz suggests they should.

Comparisons of eight parameter decompositions under synthetic data

Before comparing the different parameterizations, note that, in general, comparisons refer to any site near the perimeter of the hemisphere. Results particular to any site will be noted as such. Also, the synthetic data represent only a particular class of 3-D data, as discussed above.

Recall that the 2-D estimates of regional impedance are mixtures of the true 2-D regional impedances, because the locally *measured* electric fields are mixtures of the regional electric fields as expressed mathematically by the electric scattering or distortion operator $\underline{C}$. The algebraic estimates (Figure 10) differed from the rotated estimates (Figure 8) only in the minor impedance and then only when that impedance estimate became extremely small. The magnitudes and phases of Eggers's eigenvalues (Figure 11), LaTorraca et al.'s characteristic values (Figure 12), and Spitz's first set of eigenvalues (Figure 13) are all essentially the same as the 2-D algebraic estimates. Necessarily, the algebraic estimates of 2-D impedance and Eggers's eigenvalues will be identical since they use the same formula [equation (37)]. However, there are essentially no differences from the LaTorraca characteristic values nor from the first set of eigenvalues of Spitz due to the matrix $\mathbf{Q}$ (Figure 13).

On the other hand, the second set of eigenvalues of Spitz due to $\underline{U}$ (Figure 14) appear to recover some of the informa-

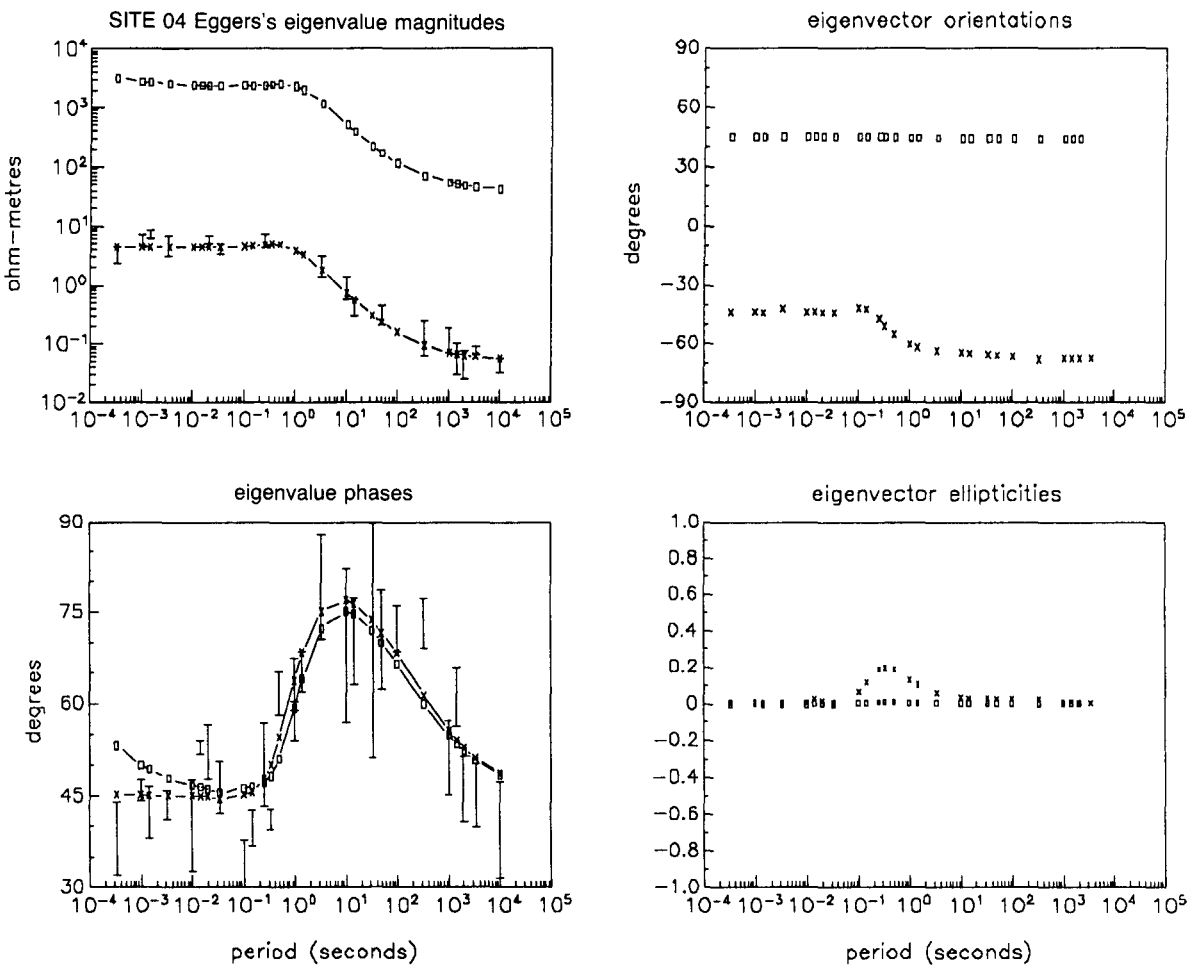

FIG. 11. Eggers's eigenvalue parameters at site 04: The two eigenvalues are represented by their scaled magnitudes (i.e., apparent resistivities) and the complex phases of the eigenvalues. The two electric eigenvector orientations and ellipticities are plotted.

tion of the regional impedances (Figure 5). This intrinsic coordinate system generally recovers the regional phases except at high frequencies where there are galvanic magnetic effects. It also recovers the shape of the regional apparent resistivities, except at high frequencies where the regional fields are essentially 1-D. However, the scaling of the magnitudes is not the same as the true regional scaling (Figure 5). In addition, the parameters recovered by Spitz's second parameterization suffer from instability with even a moderate amount of noise. In Figure 14, error bars were not placed upon the eigenvalues. At this site, these parameters were particularly erratic with noise. At other sites around

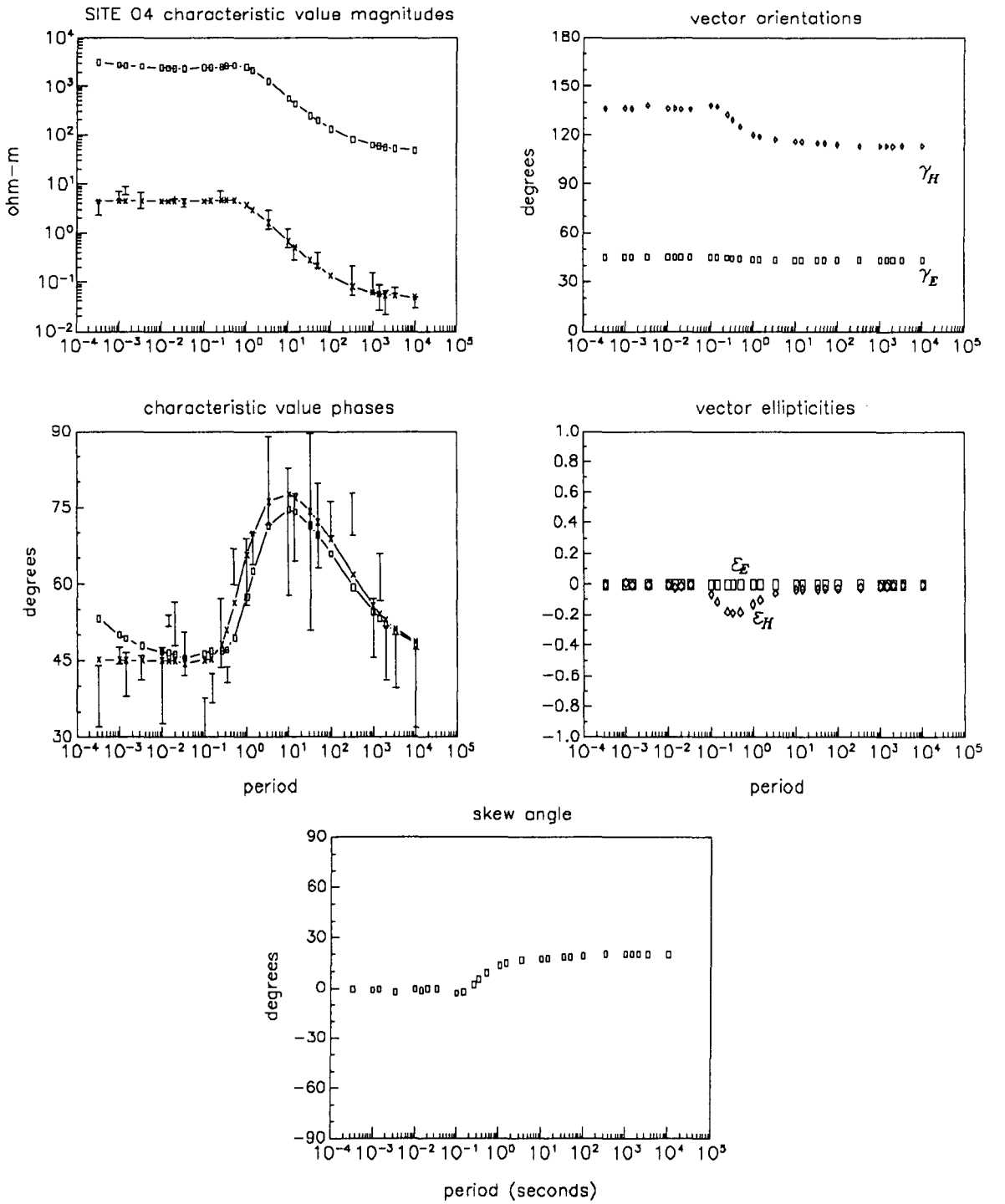

FIG. 12. Site 04: Latorraca et al. parameterization. The magnitudes of the characteristic values and their phases are plotted with the characteristic vector orientations and ellipticities. The authors' skew angle [equation (42)] is also plotted.

the hemisphere, the larger eigenvalue due to $\underline{U}$ was reasonably stable but the minor continued to be erratic. Constraining the second intrinsic angle due to $\underline{U}$ might solve some of the stability problems without loss of information.

With regard to the structural angles recovered by the various methods, Eggers's first electric eigenvector orientation (Figure 11) is almost exactly 45 degrees. This is the angle at which the site is located with respect to the center of the hemispherical inhomogeneity and the coordinate system (the symmetry axes of the 2-D regional structure). This angle

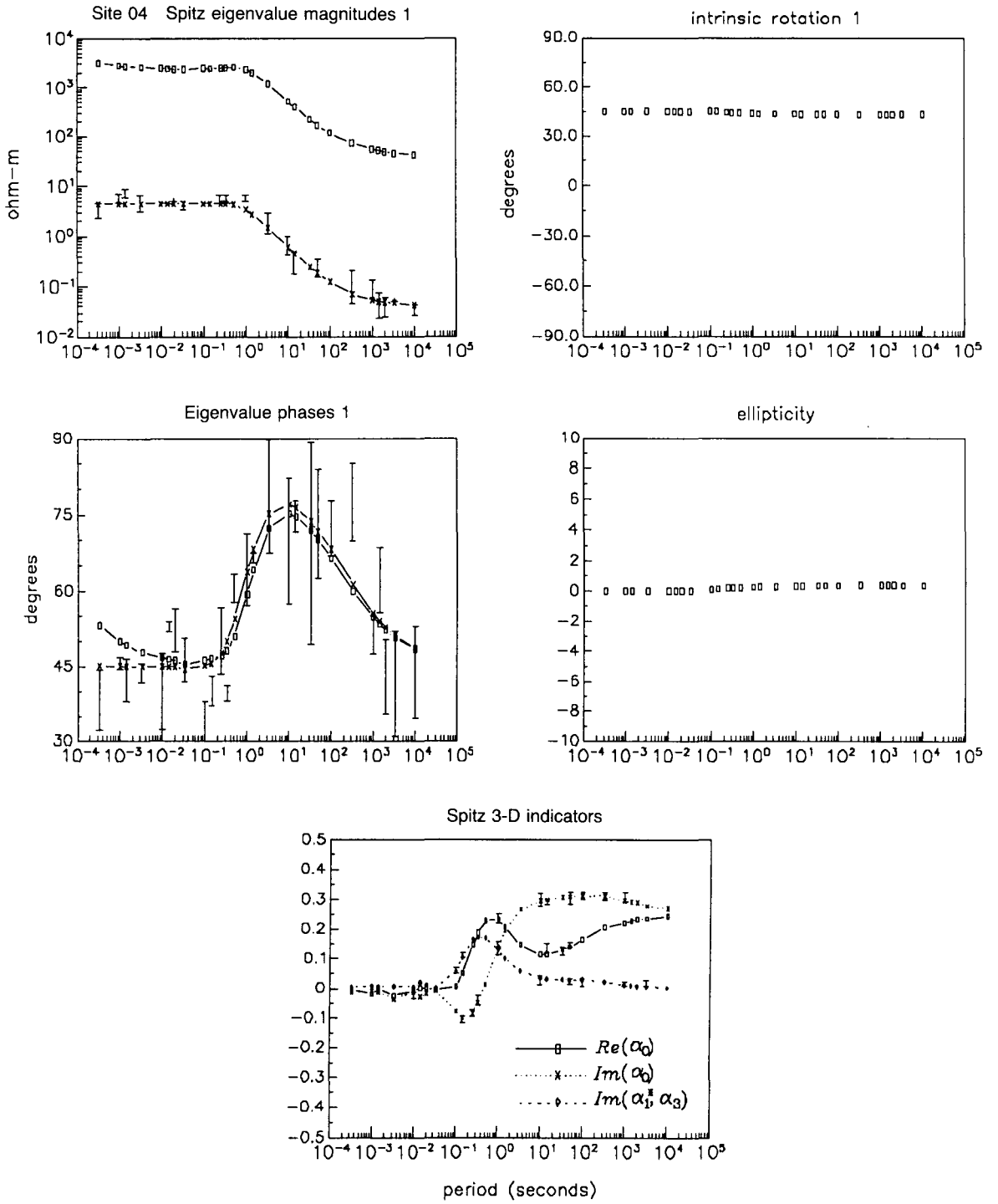

FIG. 13. Spitz parameterization due to **Q**: The intrinsic rotation angle derived from the **Q** tensor in the Cayley transformation is plotted along with the eigenvalues in that coordinate frame. Spitz's ellipticity for this orientation and his 3-D indicators are also plotted. The error bars in the eigenvalue phases are associated with the minor eigenvalue. The errors in the other phase, the rotation angle, and ellipticity are too small to be evident.

is also the azimuth of the local current at high frequencies and the high-frequency estimate of 2-D strike (Figure 8) by the conventional method. LaTorraca et al.'s orientation of the electric characteristic value (Figure 12) is also 45 degrees as is Spitz's first intrinsic orientation (Figure 13) due to the matrix **Q**. At about 10 Hz, the regional impedances begin to split (Figure 5) due to the two-dimensionality. Simultaneously, the 2-D estimate of strike (Figure 8) begins to vary slowly from 45 degrees to its low frequency asymptote which it reaches by 1 Hz. This range (1–10 Hz) is the range over which the 2-D impedances (Figure 5) have their largest phase differences and the greatest differences in the shapes of the apparent resistivity curves. At 10 Hz, Eggers's second eigenvector orientation changes through one decade from -45 degrees to an angle just slightly more than 90 degrees different from the long period conventional estimate of strike (Figure 8). LaTorraca's (Figure 12) magnetic orientation γ_H is almost exactly π radians different from Eggers's second electric orientation. Spitz's second intrinsic orientation, however, is peculiar quite apart from it being unstable both with noise and at high frequencies where there is no natural regional orientation. This second azimuthal orientation, instead of being close to $\pi/4 \pm \pi/2$, is closer to 0 degrees which is the correct regional strike for this data. However, at long periods it is systematically different from zero by about 10 degrees. This intrinsic angle systematically changes with site but is always relatively close to 0 degrees and usually quite erratic when noise is added.

Eggers's first ellipticity, LaTorraca's electric ellipticity ε_E, and Spitz's first ellipticity are all almost identically zero at all sites suggesting linear polarization. At site 01, the second ellipticity of all methods is identically zero. As one rotates the site around the hemisphere, this second ellipticity increases in magnitude to a maximum at site 04. However, they are nonzero only over the range 1 to 10 Hz, where the most significant 2-D induction is taking place (Figure 5). The ellipticity of LaTorraca is the negative of Eggers since a direction is also associated with it. Spitz's second ellipticity (Figure 14) does not have the same shape as the other two nonzero ellipticities but rather appears more like a spike.

We briefly summarize the site-to-site comparisons. The strength of the local current distortion naturally falls off with distance from the center of the hemisphere [equation (6)] and thus the mixing of the regional electric fields into the local electric fields decreases with distance. As a result, the mixing of the regional impedances in the eigenvalues and

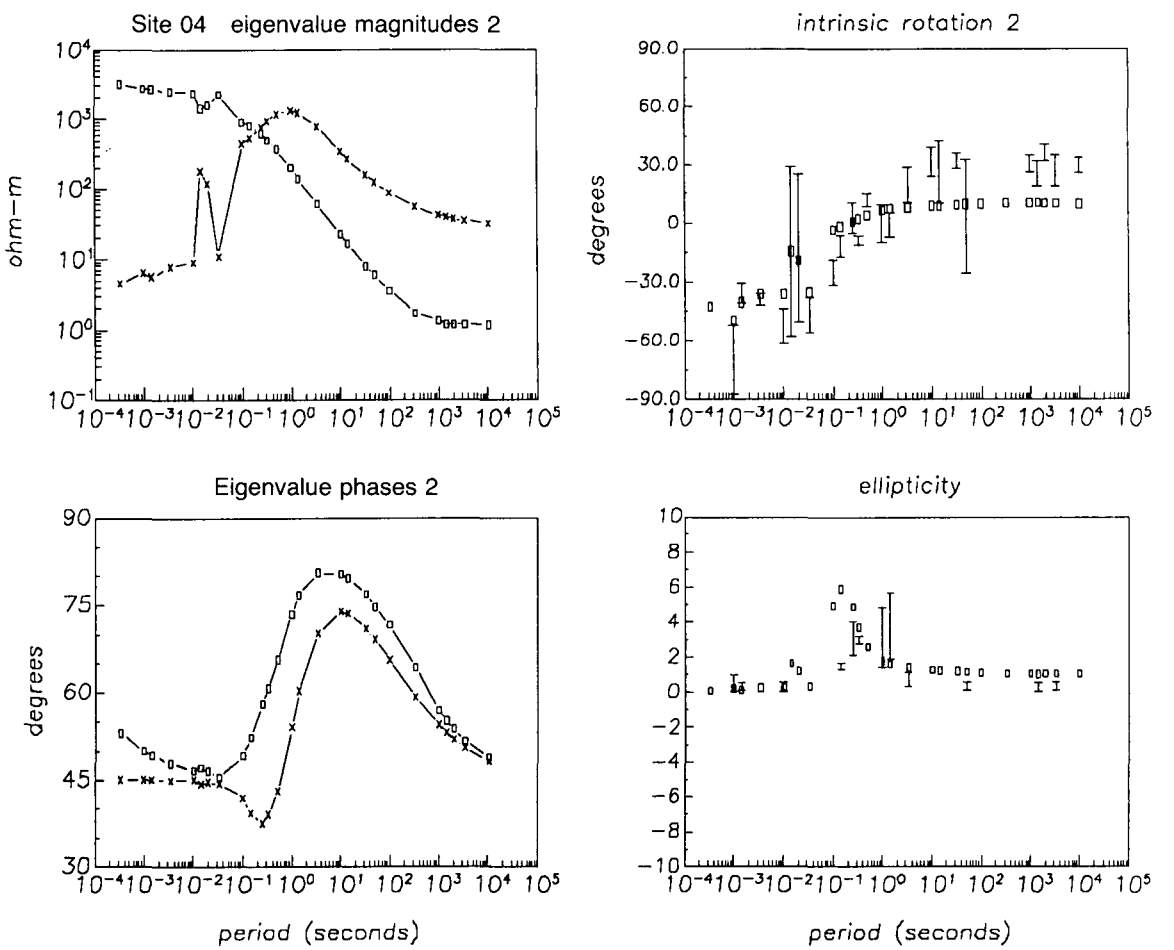

FIG. 14. Spitz parameterization due to **U**: The intrinsic rotation angle derived from the **U** tensor in the Cayley factorization is plotted along with the eigenvalues in that coordinate system. The associated ellipticity is plotted. Due to their large size, the errors are omitted for both eigenvalue magnitude and phase.

characteristic values decreases also with distance. For a fixed radial distance, the impedance estimates for Eggers, LaTorraca, Spitz, the 2-D algebraic, and the conventional rotated results are similar for all the sites. The degree of mixing of the regional impedances is dependent, however, upon the site from a minimum on the principal axes (site 01) to a maximum at 45 degrees from these axes (site 04). The amount of mixing increases rapidly as one moves off the principal axis and then slows as one approaches the lines $|y| = |x|$. For the azimuthal orientations at all sites, the angles determined from these four methods have the same similarities as at site 04. The angle which is recovered is approximately the angle θ of the site's orientation in the regional coordinate frame. The first ellipticity of Eggers and Spitz and the electric ellipticity of LaTorraca et al. are always nearly identically zero. The second ellipticity is nonzero only over the range 1–10 Hz. However, the amount of excursion from zero is dependent upon site. At site 01, for example, the second ellipticity is zero at all periods. Spitz's second orientation always recovers some of the information of the regional structure. That is, it appears to unmix the impedance data to recreate some of the information in the regional impedances. The amount of instability with noise in Spitz's second impedance estimate is dependent upon the site.

Except for Spitz's second factorization, the impedance parameters from the different methods are very similar to the rotated 2-D estimates except when the rotated estimates become unstable with noise. In general, they still suffer from mixing of the regional responses. All three methods provide an angular orientation which is dependent only upon the geometry of the 3-D inhomogeneity. The second orientation of both Eggers and LaTorraca et al. are strongly related to the principal strike direction as determined via Swift. This latter angle appears to be strongly determined by the local current polarization angle. In each method, one ellipticity is essentially zero (linear polarization) while the second is significantly nonzero only at those periods where there is strong 2-D induction present. Although this ellipticity may be nonzero for 3-D induction as well, we could not test this here.

Galvanic distortion decomposition

We recently presented a decomposition method (Groom and Bailey, 1989) which was specifically designed to deal with the problem of low-frequency 3-D electric distortions as created by our model. In our earlier paper, we showed that an arbitrary real 2×2 electric scattering or channeling tensor (i.e., for any geometry of local inhomogeneity), $\underline{C}$ can always be written as a product factorization of three basic suboperators

$$\underline{C} = g\underline{T}\underline{S}\underline{A}.$$

The suboperators have the form

$$\underline{T} = g_T\begin{bmatrix} 1 & -t \\ t & 1 \end{bmatrix}, \quad \underline{S} = g_S\begin{bmatrix} 1 & e \\ e & 1 \end{bmatrix}, \quad \underline{A} = g_A\begin{bmatrix} 1+s & 0 \\ 0 & 1-s \end{bmatrix}$$

and are called twist, shear, and anisotropy, respectively. The factor g is a scalar "site gain." Recall that at site 01, $\underline{C}$ had the form of $\underline{A}$ [equation (14)] or $e = t = 0$, while at site 04, $\underline{C}$ has the form of $\underline{S}$ [equation (16)] or $s = t = 0$.

The anisotropy operator $\underline{A}$ is incorporated into the regional impedance tensor and combines regional anisotropy with any local anisotropy which has the same strike as the regional strike. The impedance tensor is therefore modelled by the form

$$\hat{\underline{Z}} = \underline{R}(\theta)\underline{T}\underline{S}\hat{\underline{Z}}_2\underline{R}^T(\theta) \tag{46a}$$

where

$$\hat{\underline{Z}}_2 = g\begin{bmatrix} 0 & (1+s)Z_\perp \\ -(1-s)Z_\parallel & 0 \end{bmatrix} \tag{46b}$$

and $Z_\perp$ and $Z_\parallel$ are the actual 2-D impedances [equation (18)].

This method then simultaneously extracts estimates of the distortion parameters t and e, the regional strike (θ), and the modified 2-D regional impedances either by analytic solution or least-squares fitting of the model to the data. In a least-squares fit, any of the model parameters can be constrained. (In Figure 16, for example, the regional azimuth or strike has been constrained.) For site 04, the extracted principal impedances and the regional strike are plotted along with the arctangent of the twist and shear parameters as angles (Figures 15 and 16). The least-squares error of fit [equation (27)] of the resulting parameters under the model [equations (46)] to the data is also plotted.

First compare the results of an unconstrained galvanic decomposition (Figure 15) with Spitz's second orientation results (Figure 14). Note the similarities in the impedance magnitudes and phases (errors excluded). Without noise, the regional phases are recovered by both methods (except where galvanic magnetic effects are present). Both methods also recover the regional apparent resistivity shapes when there is a significant effect due to the regional two-dimensionality. The Groom-Bailey method recovers (in the absence of noise) the correct regional strike at long periods. At short periods, the effect of the regional strike on the data is minimal (i.e., buried in the noise). Also note that the Groom-Bailey method recovers an estimate of local current azimuth (Groom and Bailey, 1989).

Without noise, the channeling parameters (twist and shear) at long periods (>0.1 s) are recovered correctly (Figure 15). Using an analytic solution (Groom and Bailey, 1989), the channeling or distortion matrix for this site was shown to have a shear of 42.5 degrees and a twist of 0 degrees. At this site, however, determination of these parameters is extremely unstable in the presence of noise. At other sites, the regional azimuth, channeling parameters, and impedances are more and more stable as the shear angle for the site becomes smaller. For example, at other sites, the true frequency-independent regional strike can be inferred quite simply since scatter in this parameter is so small. However, at site 04, due to the near-simplicity of $\underline{Z}$ it can be sought only by testing for a minimum average rms error for a fixed frequency-independent strike.

Once the regional strike is constrained to be the correct value (i.e., zero), we recover the remainder of the parameters with very small scatter (Figure 16). The local current strike is recovered as 45 degrees. This is the orientation of Eggers's first electric eigenvector and LaTorraca et al.'s electric characteristic vector. It is also the value of Spitz's first intrinsic orientation, the short-period conventional 2-D strike, and the actual short-period current azimuth. The values determined for twist and shear are the correct values and the

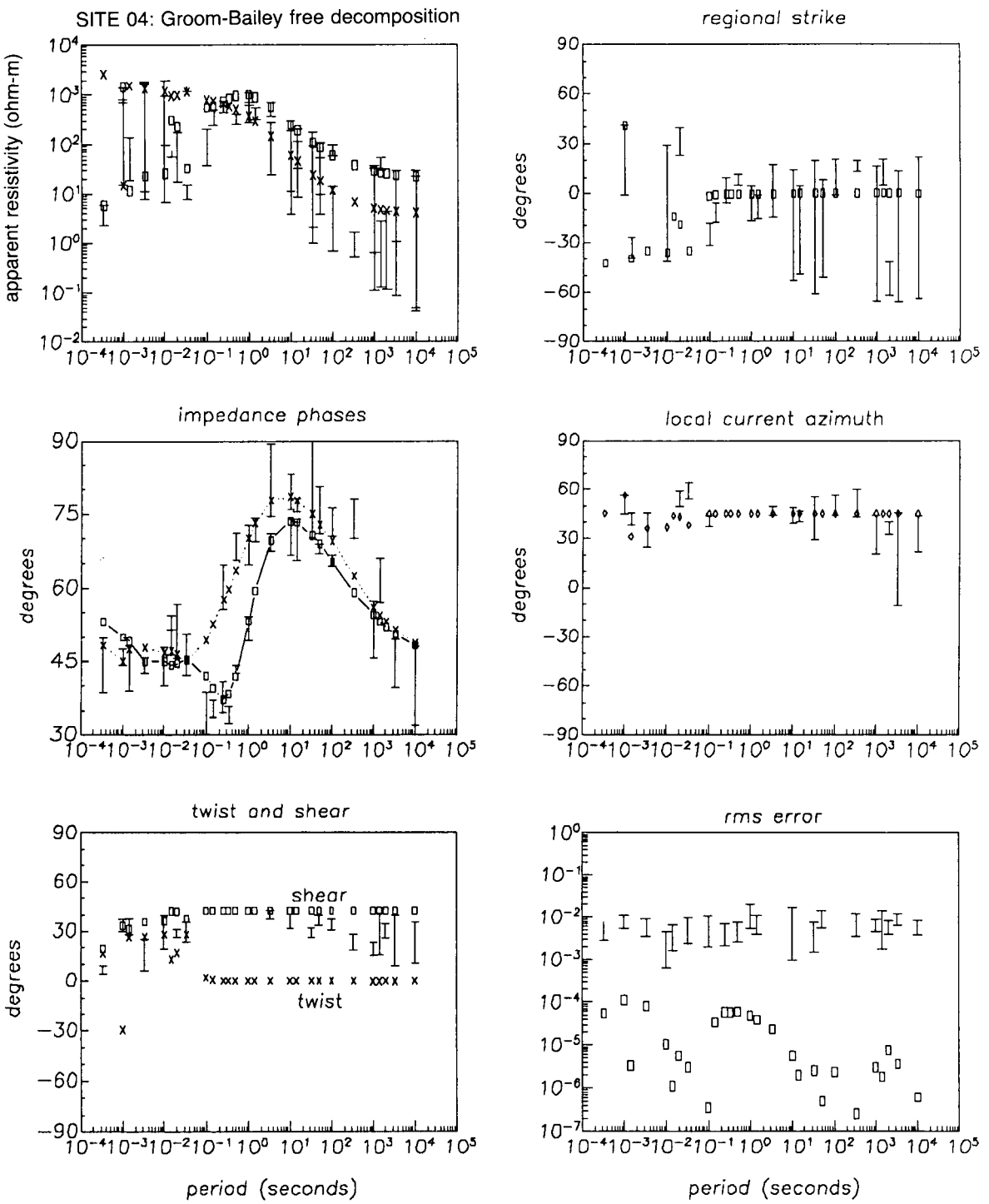

FIG. 15. Site 04: Groom-Bailey unconstrained decomposition. The Groom-Bailey parameters with no constraints are plotted for the site 04 data. For clarity, the error bars for the twist parameter are not plotted. These error bars are very similar in size to those for shear.

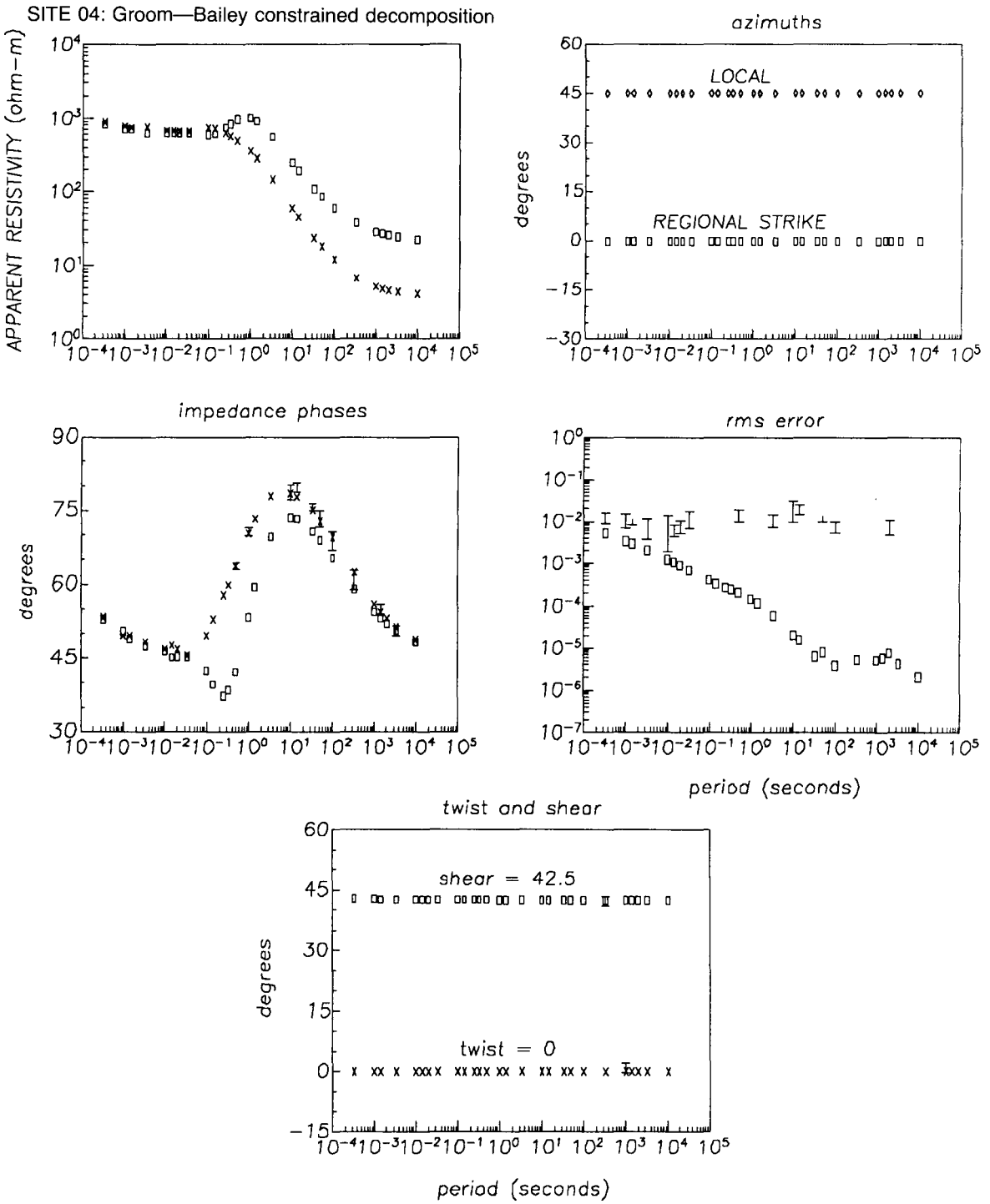

FIG. 16. Site 04: GB constrained parameters. The Groom-Bailey parameters are plotted with errors when the solution is constrained such that the regional strike is zero. No other constraints are made and the error bars are included for all parameters.

impedance phases are the phases of the regional impedances except in the short periods where there are some galvanic magnetic effects. The method recovers the correct shapes of the regional apparent resistivities but scaled by a static site gain.

In summary, there are many similarities in the parameters recovered by this method designed specifically for the type of conductivity model used here and Spitz's second intrinsic system ($\underline{\mathbf{U}}$). The parameters recovered by our channeling decomposition can be unstable with the addition of signal noise. In this case, constraining the regional strike enables the stable recovery of the correct regional impedance phases, the correct shapes of the regional apparent resistivities, and the correct values of the distortion parameters, twist, and shear. An accurate estimate of the orientation of the major axis of the current ellipse (local strike) can be found when the shear value is large [$e = O(1)$].

Although the practical use of this method is not the subject of this paper, some comments are warranted regarding the two frequency-independent scalars (s, g) which can cause shifts in the recovered apparent resistivity curves. In general, the two apparent resistivity curves are shifted by different amounts. In many practical cases, the underlying 2-D structure of interest does not affect the data at the highest frequencies at least for some sites. This is the case for the synthetic data set. When this type of structure occurs, all anisotropy (splits) in the high-frequency decomposition-recovered apparent resistivities are due to the local near-surface structure. The anisotropy or splitting factor (s) can then be estimated and removed from the apparent resistivity estimates at all frequencies. The impedance estimates now contain good estimates of the regional phase responses and the correct relative apparent resistivities. That is, the apparent resistivity curves have the correct shape and they are now both shifted by the same factor (g). Whether by controlled source EM methods, correlation with seismic contacts, or other a priori knowledge, this factor must be determined by some means other than the individual site MT data. A more complete discussion of these and other questions regarding the practical use of distortion decompositions is reserved for a future paper.

CONCLUSIONS

In the presence of a small 3-D inhomogeneity, the 2-D parameterization mixes the regional responses. The amount of mixing is site dependent. The eigenvalues of Eggers, the characteristic values of LaTorraca et al., and the eigenvalues of Spitz's first orientation ($\mathbf{Q}$) are virtually identical and they are also the same mixtures as the 2-D estimates of impedance. The second orientation of Spitz ($\underline{\mathbf{U}}$) and the Groom-Bailey method can recover much of the regional impedance information correctly. For some sites, both of these methods can be somewhat unstable in their estimation of impedance parameters in the presence of noise. Presently, only the Groom-Bailey method has the ability to constrain the regional strike to recover more stable estimates of impedance, but possibly Spitz's second orientation could similarly be constrained to reduce the scatter in the other parameters.

For the 2-D regional induction case, only the Groom-Bailey method is able to recover, independent of the site, the correct regional strike. The azimuthal directions recovered by the other methods generally recover the azimuthal position of the site which, due to the symmetry of the hemisphere, is also the current polarization azimuth. The second orientation of Spitz is close to the regional strike but consistently in error by 10 to 20 degrees. One of the ellipticities recovered by Eggers, LaTorraca et al., and Spitz is identically zero while the other differs from zero only when there are significant differences in the phases of the regional impedances (i.e., strong 2-D inductive effects).

ACKNOWLEDGMENTS

We wish to thank Drs. D. Boerner, A. G. Jones, G. Jiracek, and R. Kurtz for many helpful comments and suggestions. Geological Survey of Canada contribution no. 36989.

REFERENCES

Bahr, K., 1988, Interpretation of the magnetotelluric impedance tensor: regional induction and local telluric distortion: J. Geophys., **62**, 119–127.

Bannister, P. R., 1966, Quasi-static fields of dipole antennas at the earth's surface: Radio Sci., **1**, 1321–1330.

Berdichevsky, M. N., and Dmitriev, V. I., 1976, Basic principles of interpretation of magnetotelluric curves, *in* Adam, A., Ed., Geoelectric and geothermal studies: Akademini Kiado, 165–221.

Edwards, R. N., Lee, H., and Nabighian, M. N., 1978, On the theory of magnetometric resistivity (MMR) methods: Geophysics, **43**, 1176–1203.

Eggers, D. E., 1982, An eigenstate formulation of the magnetotelluric impedance tensor: Geophysics, **47**, 1204–1214.

Groom, R. W., 1988, The effects of inhomogeneities on magnetotellurics: Ph.D. thesis, Univ. of Toronto.

Groom, R. W., and Bailey, R. C., 1989, Decomposition of magnetotelluric impedance tensors in the presence of local three-dimensional galvanic distortion: J. Geophys. Res., B, **93**, 1913–1925.

Honkura, Y., 1975, Perturbation of the electric current by a resistivity anomaly and its application to earthquake prediction: J. Geomag. Geoelectr., **28**, 47–57.

Jiracek, G., 1990, Near surface and topographic distortion in electromagnetic induction: Surveys in Geophysics.

LaTorraca, G. A., Madden, T. R., and Korringa, J., 1986, An analysis of the magnetotelluric impedance for three-dimensional conductivity structures: Geophysics, **51**, 1819–1829.

Lee, H., 1975, On the computational aspects of magnetometric resistivity and its application to the mapping of a sink: PhD thesis, Univ. of Toronto.

Madden, T. R., and Thompson, W., 1965, Low frequency electromagnetic oscillations of the earth-ionosphere cavity: Rev. Geophys., **3**, 211–254.

Park, S. K., 1985, Distortion of magnetotelluric sounding curves by three-dimensional structures: Geophysics, **50**, 785–797.

Spitz, S., 1985, The magnetotelluric impedance tensor properties with respect to rotations: Geophysics, **50**, 1610–1617.

Swift, C. M., Jr., 1967, A magnetotelluric investigation of an electrical conductivity anomaly in the southwestern United States: Ph.D. thesis, Mass. Inst. of Tech.

Ward, S. H., 1967, Electromagnetic theory for geophysical applications, *in*, Mining Geophysics: Soc. Explor. Geophys., vol. 2, 10–196.

West, G. F., and Edwards, R. N., 1985, A simple parametric model for the electromagnetic response of an anomalous body in a host medium: Geophysics, **50**, 2542–2559.

Yee, E., and Paulson, K. V., 1987, The canonical decomposition and its relationship to other forms of magnetotelluric impedance tensor analysis: J. Geophys., **61**, 173–189.

Zhang, P., Roberts, R. G., and Pedersen, L. B., 1987, Magnetotelluric strike rules: Geophysics, **51**, 267–278.

APPENDIX

ANOMALOUS MAGNETIC FIELD DUE TO THE CONDUCTING HEMISPHERE

The solution for the galvanically distorted electric fields due to the hemisphere [equations (5) and (6)] provides the means for determining the effects of the hemisphere on the magnetic field. The source of this anomalous electrostatic magnetic field is the anomalous current density $\mathbf{J}_a$ within all of the conducting half-space including the conducting hemisphere. The anomalous magnetic field at any field point is given by the Biot-Savart law as

$$\mathbf{H}_a(x_0, y_0, z_0) = \frac{1}{4\pi} \int \frac{\mathbf{J}_a(x, y, z) \times \hat{\mathbf{r}}}{r^2}\, dV, \qquad \text{(A-1)}$$

where $\mathbf{r} = r\hat{\mathbf{r}}$ is the vector from $\mathbf{J}_a\, dV$ to the field point (x_0, y_0, z_0) and the integral is over the half-space $z > 0$.

The anomalous current density within the hemisphere, given by

$$\mathbf{J}_a = \sigma_2 \mathbf{E} - \sigma_1 \mathbf{E}_0,$$

is constant [equation (5)] as

$$\mathbf{J}_a = \frac{2\sigma_1(\sigma_2 - \sigma_1)}{\sigma_2 + 2\sigma_1} E_0 \hat{\mathbf{x}}.$$

The anomalous magnetic field due to the anomalous currents in the hemisphere $\mathbf{H}_H$ is therefore

$$\begin{aligned}\mathbf{H}_H(x_0, y_0, z_0) &= \frac{2\sigma_1(\sigma_2 - \sigma_1)}{\sigma_2 + 2\sigma_1} \frac{E_0}{4\pi} \int_{V_H} \frac{\hat{\mathbf{x}} \times \hat{\mathbf{r}}}{r^2}\, dV \\ &= \frac{2\sigma_1(\sigma_2 - \sigma_1)}{\sigma_2 + 2\sigma_1} \frac{E_0}{4\pi} \\ &\quad \times \int_{V_H} \frac{(z - z_0)\hat{\mathbf{y}} + (y_0 - y)\hat{\mathbf{z}}}{[(x - x_0)^2 + (y - y_0)^2 + (z - z_0)^2]^{3/2}}\, dV,\end{aligned} \qquad \text{(A-2)}$$

where V_H is the volume of the hemisphere.

To determine the magnetic field due to the anomalous current outside the hemisphere, we use a vector identity (Lee, 1975):

$$\begin{aligned}\frac{\mathbf{J}_a(x, y, z) \times \hat{\mathbf{r}}}{r^2} &= \nabla_0 \left(\frac{1}{r}\right) \times \mathbf{J}_a(x, y, z) = \nabla_0 \times \left(\frac{\mathbf{J}_a}{r}\right) \\ &= \frac{\nabla \times \mathbf{J}_a(x, y, z)}{r} - \nabla \times \left(\frac{\mathbf{J}_a(x, y, z)}{r}\right)\end{aligned} \qquad \text{(A-3)}$$

where again $\hat{\mathbf{r}} = \mathbf{r}/r$ is the unit vector pointing from the source point (x, y, z) to the field point (x_0, y_0, z_0), ∇_0 is an operator with respect to the field points, and ∇ is an operator with respect to source points. Since the anomalous currents are static, outside the hemisphere

$$\nabla \times \mathbf{J}_a(x, y, z) = \sigma_1 \nabla \times \mathbf{E}_a(x, y, z) = 0. \qquad \text{(A-4)}$$

Therefore the magnetic field from the anomalous currents outside the hemisphere $\mathbf{H}_E$ is given by

$$\begin{aligned}\mathbf{H}_E(x_0, y_0, z_0) &= \frac{-1}{4\pi} \int_V \nabla \times \left[\frac{\mathbf{J}_a(x, y, z)}{r}\right] dV \\ &= \frac{1}{4\pi} \int_{S_1 \cup S_2} \frac{\mathbf{J}_a(x, y, z)}{r} \times \mathbf{da}\end{aligned} \qquad \text{(A-5)}$$

utilizing a volume-to-surface integral transformation. The vector **da** has magnitude da and is in the direction of the outward normal to the surface. The surface integral is over two surfaces:

$$S_1 = \{(x, y, z) | \, z = 0, \sqrt{x^2 + y^2} > R\} \qquad \text{(A-6a)}$$

$$S_2 = \{(x, y, z) | \, z \geq 0, \sqrt{x^2 + y^2 + z^2} = R\}. \qquad \text{(A-6b)}$$

S_1 is the surface of the conducting half-space outside the hemisphere and S_2 is the radial surface of the hemisphere.

On S_2, **da** is normal to the hemisphere and points toward the origin. Thus

$$\begin{aligned}\mathbf{J}_a \times \mathbf{da} &= \frac{\sigma_1 P}{R^5} (2x^2 - y^2 - z^2, 3xy, 3xz) \times \frac{-da}{R} (x, y, z) \\ &= \frac{-\sigma_1 P da}{R^4} [0, z, -y]\end{aligned} \qquad \text{(A-7)}$$

and the contribution to $\mathbf{H}_E$ due to the surface integral over S_2, $\mathbf{H}_E^2$, is given by

$$\begin{aligned}\mathbf{H}_E^2(x_0, y_0, z_0) &= -\frac{\sigma_1 P}{4\pi R} \int_0^{2\pi} \int_0^{\frac{\pi}{2}} \frac{\cos\theta \sin\theta \hat{\mathbf{y}} - \sin\phi \sin^2\theta \hat{\mathbf{z}}}{r(\theta, \phi)}\, d\theta\, d\phi\end{aligned} \qquad \text{(A-8)}$$

where

$$\begin{aligned}r^2(\theta, \phi) = R^2 + r_0^2 - 2r_0 R[&\cos\theta \cos\theta_0 \\ &+ \cos(\phi - \phi_0) \sin\theta \sin\theta_0].\end{aligned}$$

On the surface S,

$$\begin{aligned}\mathbf{J}_a \times \mathbf{da} &= \sigma_1 \mathbf{E}_a \times \mathbf{da}(0, 0, 1) \\ &= \sigma_1 da(E_y^a, -E_x^a, 0).\end{aligned}$$

The contribution to the magnetic field from the integral over S_1, $\mathbf{H}_E^1$, is therefore

$$\begin{aligned}\mathbf{H}_E^1(x_0, y_0, z_0) &= \frac{\sigma_1}{4\pi} \int_{S_1} \frac{E_y^a(x, y, 0)\hat{\mathbf{x}} - E_x^a(x, y, 0)\hat{\mathbf{y}}}{r}\, da \\ &= \frac{\sigma_1 P}{4\pi} \left[\int_R^\infty \frac{1}{\rho^2} \left(\int_0^{2\pi} \frac{3\cos\phi \sin\phi}{r}\, d\phi \hat{\mathbf{x}}\right.\right. \\ &\quad \left.\left. - \int_0^{2\pi} \frac{2\cos^2\phi - \sin^2\phi}{r}\, d\phi \hat{\mathbf{y}}\right) d\rho\right],\end{aligned} \qquad \text{(A-9)}$$

where

$$r^2(\theta, \phi) = \rho^2 + r_0^2 - 2r_0\rho[\cos(\phi - \phi_0)\sin\theta_0]$$

and

$$\rho^2 = x^2 + y^2.$$

The horizontal magnetic field, $\mathbf{H}_h^a$, is given by equations (A-2), (A-8), and (A-9) as

$$\mathbf{H}_h^a = \mathbf{H}_{H_y} + \mathbf{H}_{E_y}^2 + \mathbf{H}_E^1, \tag{A-10a}$$

where $\mathbf{H}_{H_y}$ and $\mathbf{H}_{E_y}^2$ are the y components of $\mathbf{H}_H$ and $\mathbf{H}_E^2$, respectively. The vertical field is given by

$$\mathbf{H}_z^a = \mathbf{H}_{H_z} + \mathbf{H}_{E_z}^2. \tag{A-10b}$$

Although there may be analytic solutions to these integrals, these have not yet been found. However, all the integrals can be calculated numerically by simple means, since none of the singularities in the integrands contribute to the integral. The integral solutions show symmetries in the fields which can reduce the need for computation.

From equation (A-2) it is readily shown that $\mathbf{H}_{H_y}$ is independent of ϕ:

$$\mathbf{H}_{H_y}(\rho_0, \phi_0, \theta_0) = \mathbf{H}_{H_y}(\rho_0, \theta_0). \tag{A-11a}$$

Similarly from equation (A-8) it can be shown that

$$\mathbf{H}_{E_y}^2(\rho_0, \phi_0, \theta_0) = \mathbf{H}_{E_y}^2(\rho_0, \theta_0), \tag{A-11b}$$

whereas from equation (A-9) the y component $\mathbf{H}_E^1$, $\mathbf{H}_{E_y}^1$, is shown to have two mirror symmetries, i.e.,

$$\mathbf{H}_{E_y}^1(\rho_0, \phi_0, \theta_0) = \mathbf{H}_{E_y}^1(\rho_0, -\phi_0, \theta_0) = \mathbf{H}_{E_y}^1(\rho_0, \phi_0 + \pi, \theta_0) \tag{A-11c}$$

and thus the total horizontal y component has these symmetries. Equation (A-9) is also used to show that the x component of $\mathbf{H}_E^1$ (the only contributor to the x component of $\mathbf{H}_a$), $\mathbf{H}_{E_x}^1$, is antisymmetric about both the x-axis and the y-axis and symmetric about $|y| = |x|$, i.e.,

$$\begin{aligned}\mathbf{H}_{E_x}^1(\rho_0, \phi_0, \theta_0) &= -\mathbf{H}_{E_x}^1(\rho_0, -\phi_0, \theta_0) \\ &= \mathbf{H}_{E_x}^1(\rho_0, \phi_0 + \pi, \theta_0) \\ &= \mathbf{H}_{E_x}^1\left(\rho_0, \frac{\pi}{2} - \phi_0, \theta_0\right).\end{aligned} \tag{A-12}$$

Both contributions to the z component of the magnetic field, $\mathbf{H}_{H_z}$ and $\mathbf{H}_{E_z}^2$ have $\sin\phi_0$ symmetry [equations (A-2) and (A-8)], i.e.,

$$\mathbf{H}_z(\rho_0, \phi_0, \theta_0) = \sin\phi_0 f(\rho_0, \theta_0)\hat{\mathbf{z}}. \tag{A-13}$$

Figure 2 illustrates these symmetries. For this figure, the solutions were determined without use of the above symmetries as a check on the solution.

In the far field, the distributed dipole sources within the hemisphere will act much like a single point dipole. As such, the solutions given here should have as their limiting far-field solutions, the magnetic field due to a point electric dipole on a conducting half-space. Bannister (1966) gives the far-field solution in terms of the radial, phi, and z-components as

$$\mathbf{H}_\rho = \frac{C\sin\phi_0}{\rho^2}, \tag{A-14a}$$

$$\mathbf{H}_\phi = -\frac{C\cos\phi_0}{\rho^2}, \tag{A-14b}$$

$$\mathbf{H}_z = \frac{C\sin\phi_0}{\rho^2}, \tag{A-14c}$$

where C is a constant. Thus, in the far field, $\mathbf{H}_x$ should have $(\cos\phi_0 \sin\phi_0)$ symmetry and H_y has $(\cos^2\phi_0 - \sin^2\phi_0)$ symmetry. H_z has a $\sin\phi_0$ symmetry [equation (A-13)] even in the near field and the symmetry of H_x [equation (A-12)] is consistent with the required far-field symmetry. However, the far-field symmetry for H_y contains an additional negative mirror symmetry through the lines $|y| = |x|$ which does not appear in the nearfield [equations (A-11)]. The additional symmetry does appear in our far-field solution (e.g., Figure 2) once the integrals have been evaluated. The required far-field functional dependence of H_x on ϕ_0 [equation (A-14)] is also obtained. The far-field $\tilde{\rho}^2$ decay of H_z can be shown analytically through equations (A-2) and (A-8). That our solution satisfies the $\tilde{\rho}^2$ rate of decay for the two horizontal components was verified by evaluating the required integral solutions numerically for a variety of radial positions and different hemisphere radii (e.g., Figure 2).

We are particularly interested in the anomalous horizontal magnetic field and its effect on the impedance tensor. We can analytically determine the anomalous magnetic field at the origin (the center of the plane surface of the hemisphere), thus determining the maximum magnitude of the horizontal magnetic field (Edwards et al., 1978). Letting

$$\beta = \frac{\sigma_1(\sigma_2 - \sigma_1)}{\sigma_2 + 2\sigma_1}E_0,$$

from equation (A-2),

$$\begin{aligned}\mathbf{H}_{H_y}(0, 0, 0) &= \frac{\beta}{2\pi}\int_0^{2\pi}\int_{\frac{\pi}{2}}^{\pi}\int_0^R \sin\theta\cos\theta\, dr_s\, d\theta\, d\phi\, \hat{\mathbf{y}} \\ &= -\frac{\beta R}{2}\hat{\mathbf{y}} + 0\hat{\mathbf{z}},\end{aligned} \tag{A-15}$$

while equation (A-8) shows that at the origin,

$$\mathbf{H}_{E_y}^2(0, 0, 0) = \frac{\beta R}{4}\hat{\mathbf{y}} + 0\hat{\mathbf{z}} \tag{A-16}$$

and from equation (A-9)

$$\mathbf{H}_E^1(0, 0, 0) = -\frac{\beta R}{8}\hat{\mathbf{y}} + 0\hat{\mathbf{x}}. \tag{A-17}$$

Thus, combining equations (A-15), (A-16), and (A-17) we obtain the total anomalous magnetic field at the origin as

$$\mathbf{H}_a(0, 0, 0) = \frac{-3\beta R}{8}\hat{\mathbf{y}}. \tag{A-18}$$

Therefore,

$$|\mathbf{H}_a(x_0, y_0, 0)| \leq \frac{\sigma_1(\sigma_2 - \sigma_1)}{\sigma_2 + 2\sigma_1}\frac{E_0 R}{2}\hat{\mathbf{y}} \tag{A-19a}$$

$$= O(\sigma_1 E_0 R)\hat{\mathbf{y}} \qquad [\sigma_1 \neq \sigma_2]. \tag{A-19b}$$

When the conductivities of host and inhomogeneity are sufficiently similar, the effect of the anomalous magnetic field is obviously insignificant.

More details of the preceding analysis are given in Groom (1988).